

A dynamic window-based Euler depth estimation algorithm for potential field geophysical data

S. GHANBARIFAR¹, S.H. HOSSEINI¹, M. ABEDI² AND A. AFSHAR³

¹ *Institute of Geophysics, University of Tehran, Tehran, Iran*

² *School of Mining Engineering, College of Engineering, University of Tehran, Tehran, Iran*

³ *Department of Mining and Metallurgical Engineering, Amirkabir University of Technology, Tehran, Iran*

(Received: 6 April 2023; accepted: 9 November 2023; published online: 1 March 2024)

ABSTRACT The Euler deconvolution method is an outstanding, automatic and fast tool for depth estimation of subsurface masses in potential field geophysics. One of the main challenges in solving the standard Euler equation is accurately determining the window size, while depth estimation is essentially controlled by the variation of the assumed window size. Due to the complexity of the geological structure and targets sought, selecting the optimal fixed window size, to scan all points within the study area, is usually a difficult task. The provision of an algorithm utilising the optimal dimensions of the dynamic window, for an accurate depth calculation of the explored sources, is of particular interest for potential field geophysics. In this study, the least-squares method is used to solve the Euler equation system, control a certain error, and, at the same time, search for the optimal window size in the entire area by means of the minimum error rate. In addition to introducing a new dynamic window, this study utilises a completely new computational framework that considers an adaptive and optimal window size in order to obtain an acceptable solution from an Euler equation system. The Euler solutions for gravity and magnetic data in 3D can be visualised by exploring multiple possible window sizes to achieve ideal dimensions and minimise error values. A dynamic window-based Euler depth estimator was successfully implemented in several synthetic scenarios with different characteristics. Next, the algorithm was run on the ground magnetic and gravity data sets of the Shavaz region by depositing several iron patches. As expected, depth estimates of the underlying causative potential field anomalies were reported to be in close agreement with the drill results.

Key words: Euler depth estimation algorithm, dynamic windows, potential field data, iron deposit.

1. Introduction

The Euler depth estimator is one of the many simple and rapid techniques that have been developed to quickly define the geometry of sought sources responsible for potential field anomalies. The main advantage of this algorithm is its speed, as it efficiently provides a foundation for more in-depth and further modelling and interpretation. Due to its low processing cost, the standard Euler deconvolution approach is frequently employed in studies to evaluate potential field geophysical data. Euler equations are often used to reliably calculate the depth of subsurface sources through the horizontal and vertical derivation of the potential field. To the best of our knowledge, this method was first proposed by Thompson (1982). Detecting the depth of mineral

masses and shallow faults, calculating the depth of geothermal reservoirs, and determining the thickness of surface sediments are important applications of the Euler deconvolution method (Afshar *et al.*, 2017; Hosseini *et al.*, 2021; Ghiasi *et al.*, 2023). In addition to depth estimation, the Euler equation system can also be used to determine the anomaly boundaries and discontinuity depths (Reid *et al.*, 1990, 2014).

In the literature, attempts have been made to improve the Euler performance of depth estimation as a more refined choice and simpler method in geophysical interpretation (Guo *et al.*, 2014). In standard Euler deconvolution techniques, the structural index (SI) is a “decay power of signal” that is related to the geometric properties of the source responsible for the potential field anomalies. Depth estimation is highly dependent on the SI (Barbosa *et al.*, 1999), but can be estimated automatically by manipulating the main Euler equation and replacing the input data with the directional derivatives of the potential field data (Salem and Ravat, 2003). In fact, the analytic signal and its higher order derivatives are used here to estimate the SI . For magnetic and gravity data sets, the standard 3D Euler equations are solved by selecting the appropriate SI through a fixed window that moves across the grid. The accurate design of the window size is a key factor in successfully implementing a depth estimator (Barbosa *et al.*, 1999).

Due to the complexity of the geological structures and existence of different subsurface sources at various positions, the final depth estimates, obtained from the Euler equation, greatly depend on the window size chosen. Attention should be drawn to the fact that adjacent sources may not exactly match within the defined window. According to the described research literature, the selection of the optimal and suitable window size, necessary to solve the standard Euler equation system, has, evidently, received less attention. What is interesting here is that a dynamic window-based depth estimator is a possible scenario to strive for an accurate execution of the Euler method. However, regardless of the complexity of the computational domain, these reasons limit the application range, making it unsuitable for computing in complex environments.

In this study, in addition to presenting a new algorithm, the Euler equation system is also solved simultaneously with the minimum error for different window sizes. A more comprehensive approach is needed to thoroughly evaluate the impact of windows on depth estimates. One of the main pitfalls of the algorithm occurs when assuming a fixed window size. In the solution proposed by this study, different ranges of potential field anomalies are automatically located in dynamic windows through the search of a minimum to maximum length. Then, the most accurate responses are selected within the range of optimal window sizes. The proposed project overcomes the limitations of the standard method.

In this work, a theoretical overview is initially provided, followed, then, by experiments and numerical comparisons to validate the algorithm. Certain requirements to ensure the creation of a high-quality depth solution are necessary and will be discussed, in the following sections, by addressing numerous challenging concerns. Ultimately, the significance of this study lies in improving the performance of the Euler depth estimator by introducing and emphasising dynamic windows.

2. A dynamic window-based Euler depth estimation

This section briefly introduces the main bulk of the depth estimation algorithm (summarised in Fig. 1), and provides important preliminary information on the equation system. This section may be disregarded by the reader already familiar with this theory. In the presence of a

background field, the Euler homogeneity equation, for the magnetic and gravity potential fields, is written as:

$$(x - x_0) \frac{\partial P}{\partial x} + (y - y_0) \frac{\partial P}{\partial y} + (z - z_0) \frac{\partial P}{\partial z} = N(B - P). \tag{1}$$

Briefly describing the parameters, P is the observed magnetic or gravity field at a point (x, y, z) ; $(\partial P/\partial x, \partial P/\partial y, \partial P/\partial z)$ describe the directional derivatives of the potential fields that can be computed by means of various methods, among which convolution or Fourier domain

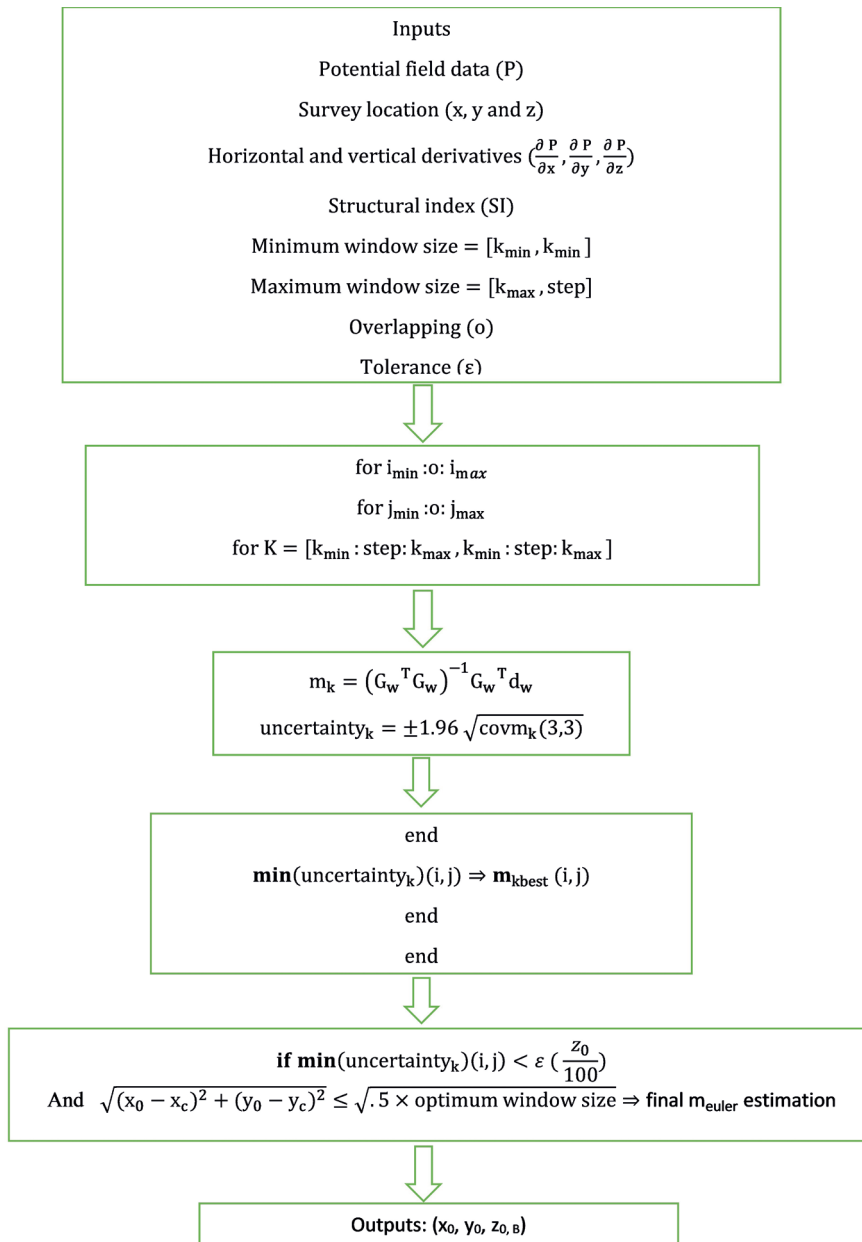


Fig. 1 - Scheme of a succinct and straight-forward procedure for coding a dynamic window-based Euler depth estimation algorithm.

computation; (x_0, y_0, z_0) delineate the location of the anomaly source (z_0 is the depth of the potential field source); B is the background or main field of the observed data; and N represents the SI , which depends on the homogeneity properties of the potential sources; SI is also the opposite of the homogeneity-degree (n). It is worth noting that for a magnetic field $N = -n$, and for gravity, N is related to n as $N = -(n-1)$; for the k -th-order field derivative of the magnetic field or of the vertical gradient of gravity $N = -(n+k)$ (Fedi *et al.*, 2015; Fedi, 2016). The SI often changes for sources of different shapes (1D, 2D, or 3D), and its determination greatly influences the final response of the Euler equation system (Reid, 2014). The basic geological information of the study area impacts on the accurate determination of this parameter in a considerable manner. Various computational methods have been developed to calculate the SI , and breakthroughs have been achieved in several studies (Barbosa *et al.*, 1999; Gerovska and Araúzo-Bravo, 2003; Salem and Ravat, 2003; Melo and Barbosa, 2018). A number of important SI s, for simple and homogeneous geological structures, are given in Table 1.

Table 1 - The SI s of some simple-shaped sources in potential field studies (Reid and Thurston, 2014).

Source	Number of infinite dimensions	Magnetic	Gravity	Depth relative to...
Sphere	0	3	2	Centre
Vertical line / pipe / cylinder	1	2	1	Top
Horizontal line / cylinder	1	2	1	Centre
Dyke	2	1	0	Top
Sill	2	1	0	Centre
Contact	3	0	-1	Top

For a single window, the simple matrix form of the linear set of Euler equations (Eq. 1), containing n observed data inside the window, is:

$$\begin{bmatrix} \frac{\partial P_1}{\partial x} & \frac{\partial P_1}{\partial y} & \frac{\partial P_1}{\partial z} & N \\ \vdots & \vdots & \vdots & \vdots \\ \frac{\partial P_n}{\partial x} & \frac{\partial P_n}{\partial y} & \frac{\partial P_n}{\partial z} & N \end{bmatrix}_{n \times 4} \begin{bmatrix} x_0 \\ y_0 \\ z_0 \\ B \end{bmatrix}_{4 \times 1} = \begin{bmatrix} \frac{\partial P_1}{\partial x}x_1 + \frac{\partial P_1}{\partial y}y_1 + \frac{\partial P_1}{\partial z}z_1 + NP_1 \\ \vdots \\ \frac{\partial P_n}{\partial x}x_n + \frac{\partial P_n}{\partial y}y_n + \frac{\partial P_n}{\partial z}z_n + NP_n \end{bmatrix}_{n \times 1} \quad (2)$$

In general, the equation system, including the foundation of the depth estimator, is written as:

$$Gm = d \quad (3)$$

$$r = d - Gm. \quad (4)$$

In this case, the solution to Eq. 3 is calculated by minimising the residual vector as follows:

$$m = G^{-1}d. \quad (5)$$

However, the most common method for finding the appropriate model parameters (m) is to minimise the second norm of the residual vector, called least squares. Due to the completeness of the statistical analyses, especially in normally distributed data sets, the least-squares method is very popular and useful for understanding the geometry of problems. To increase the certainty of the response, the minimum weighted least-squares method, one of the most widely used numerical methods in several engineering fields, is sometimes used here as $G_w m = d_w$. In such cases, the residual vector is converted into Eq. 6 [see pp. 15-30 of chapter 2 in Aster *et al.* (2018)], which shows the advantage of the data distance from the search window centre:

$$r = d_w - G_w m. \quad (6)$$

In the above-mentioned formula, $d_w = d \times W$ and $G_w = G \times W$ should be noted.

In applying the Euler equations, this study considers the weight function (W) as a diagonal matrix that is inversely related to the distance, of the observed data (s), from the centre of each window. The heaviest weight, equal to one, will be assigned to the data located in the window centre, and, as the Euclidean distance of other points increases, the weight will decrease.

$$W = \begin{pmatrix} 1/s_1 & \cdots & 0 \\ \vdots & \ddots & \vdots \\ 0 & \cdots & 1/s_n \end{pmatrix}. \quad (7)$$

Given the weight function, the simple form of the Euler equation system transforms into the following:

$$G_w m = d_w. \quad (8)$$

By multiplying the sides of Eq. 8, according to the transpose matrix of G_w , the following can be expressed:

$$G_w^T G_w m = G_w^T d_w. \quad (9)$$

Ultimately, the normal form of the equation, used to obtain the model parameter (m), can be expressed as follows [see pp. 15-30 of chapter 2 in Aster *et al.* (2018)]:

$$m = (G_w^T G_w)^{-1} G_w^T d_w. \quad (10)$$

For each data point (i, j) in the observation grid (grid nodes, hereafter), the Euler equation system is solved in the moving and dynamic square window (Fig. 2). To calculate the appropriate size of each moving window, initial minimum and maximum values are required as key steps. The square window size varies from a minimum value of $k_{min} \times k_{min}$ up to a maximum limit of $k_{max} \times k_{max}$, then, the results with the minimum uncertainty levels are chosen as the final depth solutions. Due to the complexity of various subsurface sources at different depths, the interpreter must approximate the k_{max} values, taking into account anomaly maps such as the analytic signal and edge enhancement outputs, or other geological information. According to the optimal window

size, for each grid node (i, j) , and the K -th window, the residual vector (Eq. 6) and the Euler system solution (Eq. 10) can be expressed as:

$$r_k = d_w - G_w m \quad \text{for} \quad k_{min} < k < k_{max} \quad (11)$$

$$m_k = (G_w^T G_w)^{-1} G_w^T d_w \quad (12)$$

where r_k describes the difference between the d_w observed data and the predicted data $(G_w m)$, and m_k represents the depth solutions.

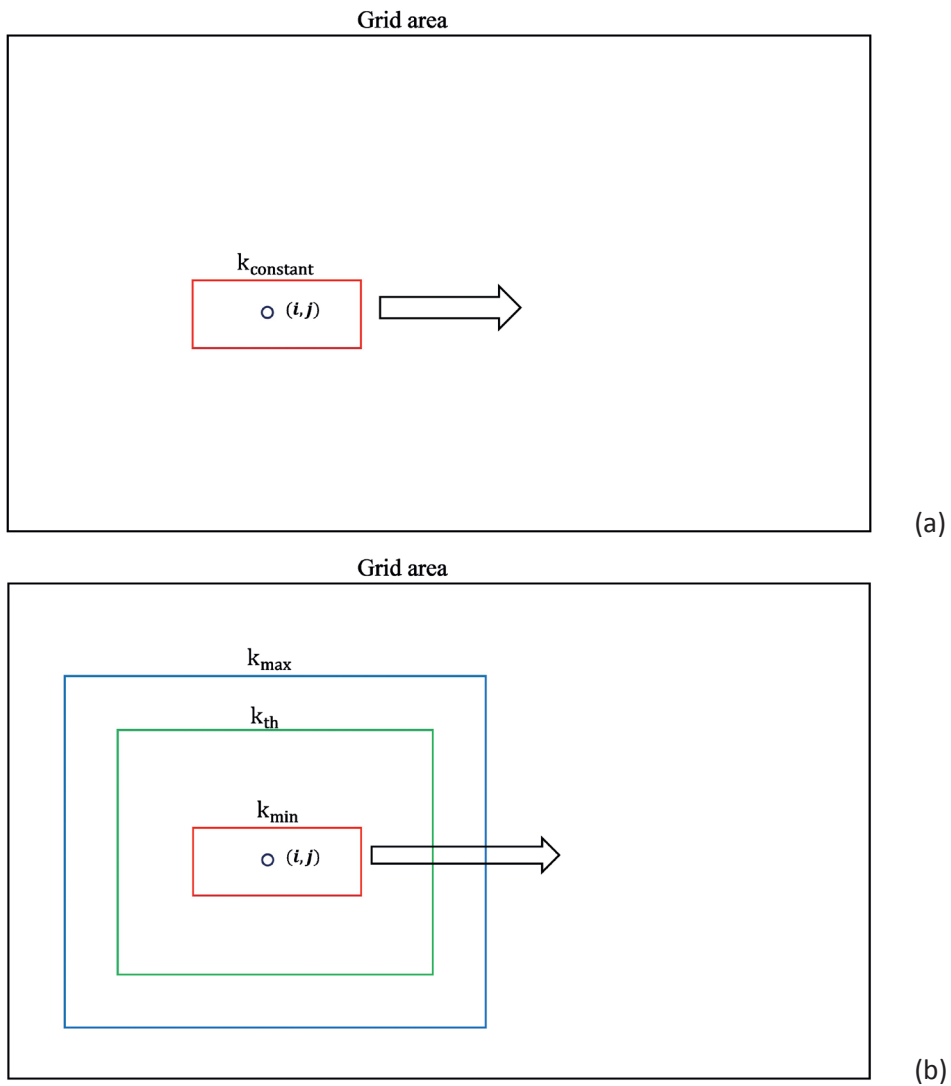


Fig. 2 - Comparison of Euler window types during grid scanning: a) fixed window, and b) dynamic window, which overcomes the limitation of the conventional Euler method to a major extent and allows substantial flexibility in searching for different sized multi-source geometries. If the distance of the survey stations (gridded area) is the same in two directions (x, y) , the searched window will be square.

Since Euler equations are solved in a moving window over the entire grid, each window provides a response. Depth, with a high degree of uncertainty, can be estimated beyond the anomaly source. Since the model parameters are usually distributed in a normal manner, to check the uncertainty level between the solutions calculated in the least-squares problem, a 95% uncertainty interval can be obtained as follows [see Aster *et al.* (2018)]:

$$uncertainty_k = \pm 1.96 \sqrt{cov(m_k)} \quad (13)$$

where, $cov(m_k)$ is the model covariance matrix for the K -th window (4×4 in size), and is calculated with the following equation [see pp. 15-30 of chapter 2 in Aster *et al.* (2018)]:

$$cov(m_k) = var(r_k)(G_W^T G_W)^{-1}. \quad (14)$$

Eventually, the model uncertainty interval for the K -th window is calculated as:

$$uncertainty_k = \pm 1.96 \sqrt{covm_k(3,3)}. \quad (15)$$

It should be noted that $covm_k(3, 3)$ is the third element of the diagonal diameter of the covariance matrix.

In the next step, for each grid node (i, j) , the optimal depth solutions are considered for the window sizes with the minimum uncertainty values:

$$\min(uncertainty_k) \Rightarrow m_{kbest} \quad (16)$$

Worthy of mention is the fact that the transition to the next window for each stage is carried out by taking into account the overlap with the previous stages.

For the entire observation grid, the set of acceptable depth solutions are those with an uncertainty that is less than the initial tolerance (e), which is also a percentage of the depth estimate. In addition to the tolerance limit, another condition for filtering an acceptable solution of the Euler equation is that the obtained positions (x_o, y_o) must lie within a closed circle of the optimal window. The obvious benefits of these constraints, in turn, yield reliable depth solutions. This condition is shown schematically in Fig. 3 (Eq. 17).

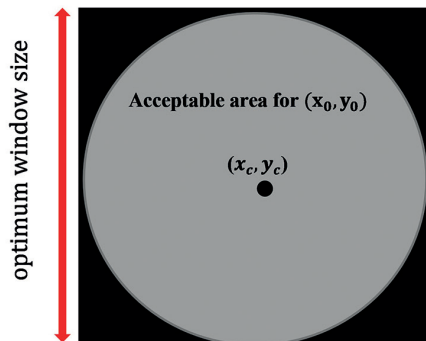


Fig. 3 - Illustrative representation of the acceptable area for filtering Euler depth estimation within an optimum window size.

In short, the set of acceptable solutions to the Euler equation can be obtained from the following conditional expression:

$$\text{if } \min(\text{uncertainty}_{y_k})(i, j) < \varepsilon \left(\frac{z_0}{100} \right)$$

$$\text{and } \sqrt{(x_0 - x_c)^2 + (y_0 - y_c)^2} \leq \sqrt{.5 \times \text{optimum window size}} \Rightarrow \quad (17)$$

final m_{euler} estimation

Fig. 3 shows a diagram illustrating the above descriptions and proposed algorithm. Based on the mathematical descriptions given above, the algorithm is, then, reviewed through the application on synthetic data and with a variety of scenarios, to further demonstrate the effectiveness and feasibility of the new proposal. However, the depth estimation methods are computationally inexpensive and allow for easy implementation of large data calculations.

3. Depth estimation of synthetic scenarios

In this section, to evaluate the effectiveness of the proposed method, the algorithm was examined for four scenarios. At each step, the potential field anomalies, generated from the synthetic models, become more complex, so as to test the proposed algorithm for different geological scenarios and find accurate windows and depth solution. Since the Euler deconvolution technique concerns homogenous sources, the algorithm was initially tested for a homogenous sphere and was, then, applied to more complex inhomogeneous synthetic bodies.

To simulate the response of synthetic magnetic and gravity field data, an area with a length and width of 1,000 m, and station spacing of 10 m, was designed. Chen and Zhang (2018) developed a forward modelling code on gravity data. By elaborating this work, magnetic and gravity data were modelled. To produce more realistic terms, the magnetic and gravity data were corrupted with 3% random Gaussian noise. These observations are, then, the inputs of the aforementioned Euler equation.

Furthermore, as noted above, Salem and Ravat (2003) reported that, through the analytic signal and its higher order derivatives, the SI , and subsurface source depths at the extremities, can be calculated from Eqs. 19 and 20, respectively. During this study, the average SI s were estimated according to the mentioned method, and, then, passed to the Euler method as a prerequisite. Additionally, estimating the depth on the analytic signal peaks will produce a view of the desired target. Following the same line of thought as Salem and Ravat (2003), the SI and z_0 are estimated at the analytic signal peak by calculating the higher order of the analytic signal amplitude (AAS). This approach provides sufficient information and valuable insight into the characteristics of the source(s). These steps were elegantly combined and, after averaging the SI estimates, they were fed into the Euler equations of the proposed method. The amplitude of the n -th-order derivative analytic signal can be expressed as:

$$|ASS_n(x, y)| = \sqrt{\left(\frac{\partial P_z^n}{\partial x}\right)^2 + \left(\frac{\partial P_z^n}{\partial y}\right)^2 + \left(\frac{\partial P_z^n}{\partial z}\right)^2} \quad (18)$$

where z denotes the vertical derivative of potential field data. The depth and SI , at the source centre, can be calculated through the following formulae:

$$SI = \left(\frac{2|AAS_1|^2 - |AAS_2||AAS_0|}{|AAS_2||AAS_0| - |AAS_1|^2} \right)_{x=x_0, y=y_0} \quad (19)$$

$$z_0 = \left(\frac{|AAS_1||AAS_0|}{|AAS_2||AAS_0| - |AAS_1|^2} \right)_{x=x_0, y=y_0} \quad (20)$$

A full discussion of the details is beyond the scope of this work and for a deeper and more rigorous description of the automatic SI estimation, in cases of limited availability of precise geological data, research by Salem and Ravat (2003), of utmost importance and deserving further investigation, is recommended. Predictably, a wrong assumption of the SI can adversely impact numerical solvers when executing the standard Euler depth estimator. However, caution should be exercised in using the estimated SI when in the presence of noise observations in the gridded data. It is worth noting that, due to intense noise impact on higher order derivatives in the Salem and Ravat (2003) method, a 20-metre upward continuation filter was applied in the Fourier domain to smooth the signals.

3.1. Homogenous spherical models

Next, depth estimation, for a homogeneous gravity and magnetic source, is performed using the dynamic window method. For this purpose, the potential field of a homogeneous source (sphere) is calculated with the coordinates of the centre, $(x_c, y_c, z_c) = (500, 500, -100)$, and a radius of 50 m (Table 2 and Fig. 4c). The magnetic susceptibility and density contrast properties of this model were 0.1 (in the SI unit) and 0.3 g/cm³, respectively. The inclination and declination angles, of the Earth's magnetic field, are assumed to be 90 and 0 degrees, respectively. As shown in Fig. 4, the magnetic and gravity fields are presented in a surface grid of 1,000 × 1,000 m² with a station spacing of 10 m, and with a 3D view of the synthetic model, and a 2D top view of the source. A summary description of the first synthetic scenario is given in Table 2.

Table 2 - Parameters assumed for the synthetic homogeneous source shown in Fig. 2.

Easting centre (m)	Northing centre (m)	Z centre (m)	Radius s (m)	Density contrast (g/cm ³)	Susceptibility (SI)	Inclination (degree)	Declination (degree)
500	500	-100	50	0.3	0.1	90	0

The depth estimation process is performed using the standard Euler algorithm, with dynamic windows ranging from a minimum of 3 to a maximum of 33 times the cell size, and considering a 1% tolerance and 90% overlap. In the next step, the depth solution is compared with the sphere centre assumed. The histogram of the estimated parameters (Fig. 5) indicates that most of the depth solutions (z_0) are found between 101 and 102 m, scattered around the location (x_0, y_0) of 500 m. However, if the average parameter value is taken as the criterion to compare the solution with the true sphere centre at coordinates $(x_c, y_c, z_c) = (500, 500, -100)$, the average values and errors obtained (Table 3) imply that the dynamic window-based method presented

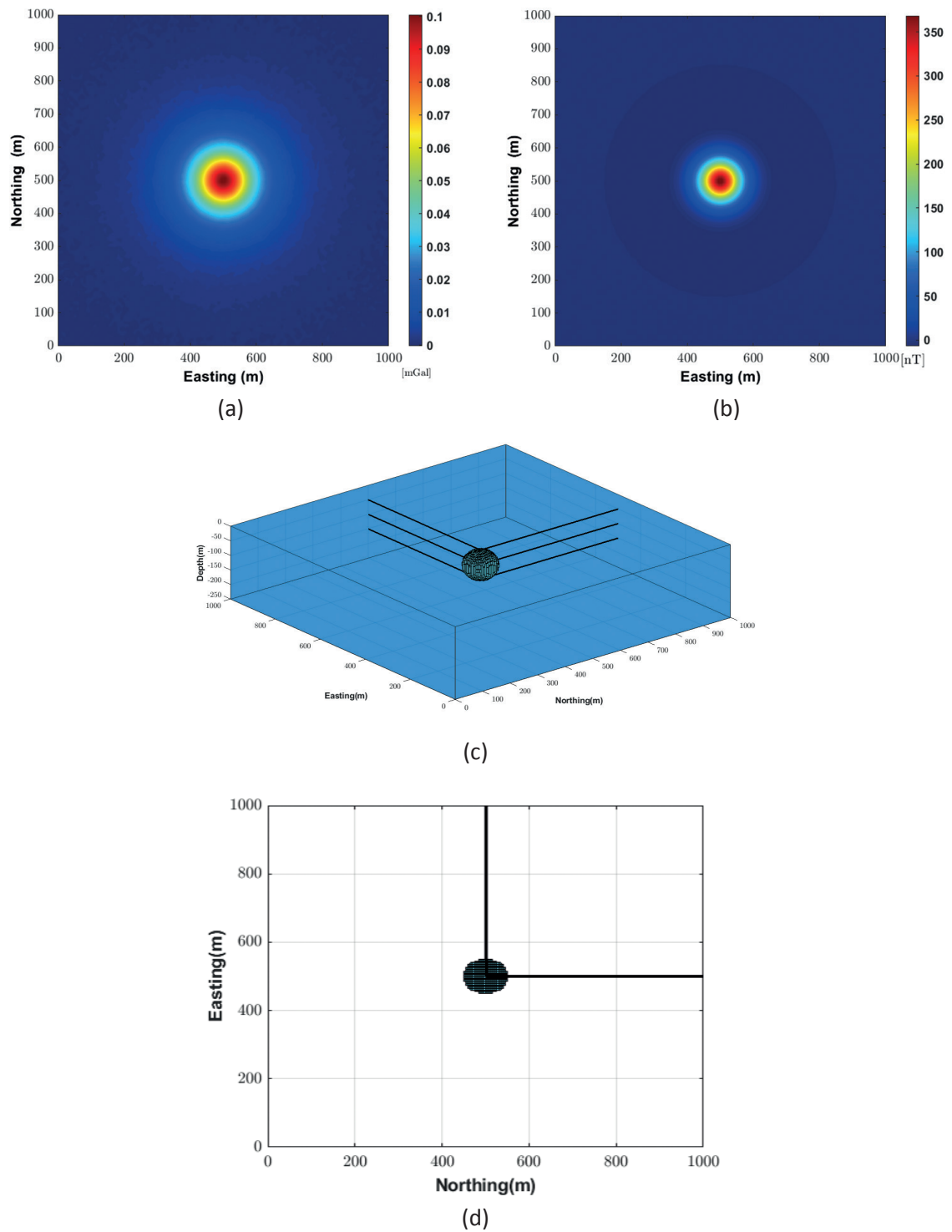
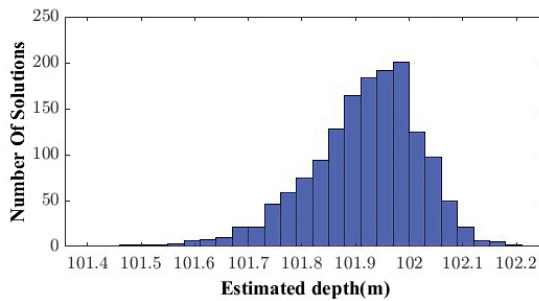


Fig. 4 - Simulation of a homogeneous source potential field anomaly: a) gravity data, b) magnetic data, c) 3D source geometry, and d) 2D top view. Synthetic magnetic and gravity data are corrupted with 3% random Gaussian noise (the black lines indicate the sphere depth and centre).

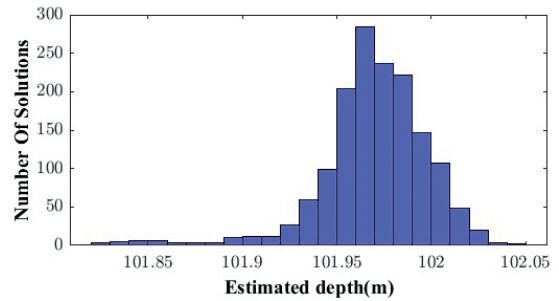
has been able to estimate the position of the homogeneous sphere in an appropriate manner. Considering small error values, the estimated mean parameters for both magnetic and gravity spherical sources were accurately recovered (Table 3).

Table 3 - The average values of the estimated parameters for the homogeneous sphere centre using the dynamic window method.

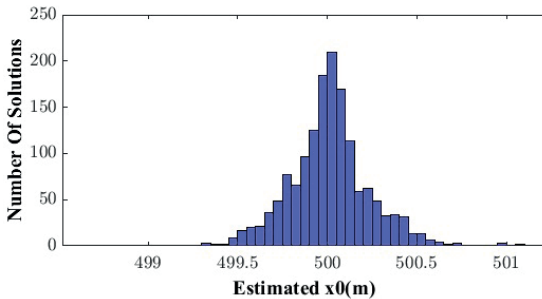
Parameters	x_0	y_0	z_0
Average estimated parameters for magnetic sphere	499.9975	500.001	101.9698
Error	0.0005	0.0002	0.9698
Average estimated parameters for magnetic sphere	500.0126	500.0054	101.9167
Error	0.0025	0.0011	0.9167



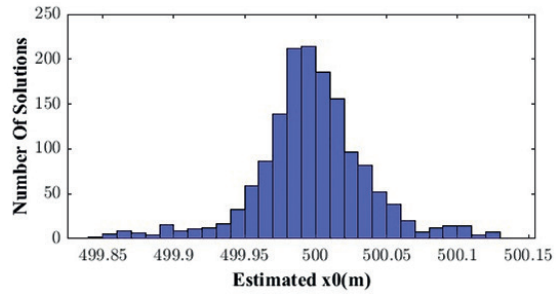
(a)



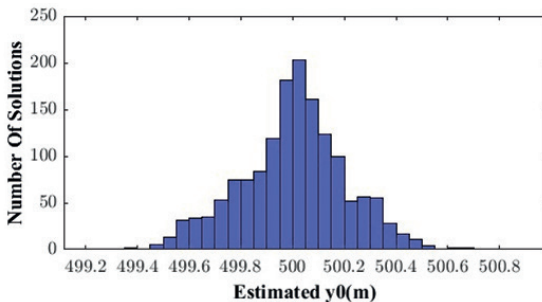
(b)



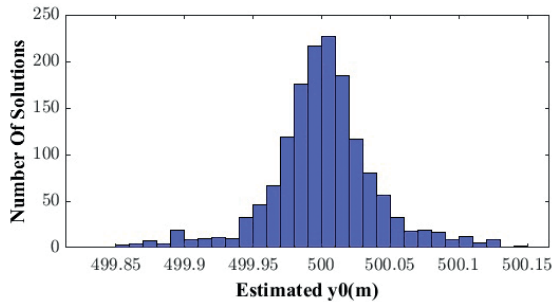
(c)



(d)



(e)



(f)

Fig. 5 - Histogram plots of the estimated parameters (x_0, y_0, z_0) for gravity and magnetic data on the left and right respectively. The physical and geometrical characteristics of the synthetic sphere source are described in Table 2.

3.2. Inhomogeneous models

3.2.1. Model 1

Using the above-mentioned forward modelling technique, a single source cuboid model was initially considered with a depth range from 50 to 150 m, a N-S elongation from 450 to 550 m, and, also, an E-W elongation from 300 to 700 m. The magnetic susceptibility and density contrast properties of this model were 0.08 (in the SI unit) and 1 g/cm^3 , respectively. The inclination and declination angles of the Earth's magnetic field are assumed to be 55 and 3 degrees, respectively. A summary description of the first synthetic scenario is given in Table 4. As shown in Figs. 6a and 6b, the magnetic and gravity field responses of the cuboid source are presented in a $1,000 \times 1,000 \text{ m}^2$ surface grid, with station spacing of 10 m. A 3D view of the synthetic model and a 2D cross-section through its midsection are shown in Figs. 4c and 4d.

Table 4 - Parameters assumed for the synthetic single source shown in Fig. 6.

Block Size (m)	Easting from to (m)	Northing from to (m)	Z from to (m)	Slope (degree)	Density contrast (g/cm^3)	Susceptibility (SI)	Inclination (degree)	Declination (degree)
100	450 550	300 700	-50	-	1	0.08	55	3
400			-150					
100								

By taking into account a similar procedure, proposed by Salem and Ravat (2003), and averaging the estimated SI at peaks above 80 nT/m for magnetic data, and 0.008 mGal/m for gravity data, the SI average equals 2.3146 and 1.2617 for the magnetic and gravity data, respectively. As previously mentioned, these values serve as the prior parameter of the Euler equation. Fig. 7 shows the depth solution of the Euler equation of the first synthetic model on the analytic signal map as well as the SI s calculated for the gravity and magnetic models. It should be noted that, by increasing the SI amount, considered as the default input to the Euler equation system (Fig. 7c), the estimated depth increases in accordance with previous studies. Therefore, the correct selection of this assumed input will have a significant impact on the estimation results.

Additionally, to implement the dynamic window method, the minimum window size is assumed to be three times greater than the observation grid cell size, so as to perform the calculations with a 90% overlap. The maximum value for the window sizes is also 33 times greater than the cell size. The 3% (ϵ) tolerance condition is also applied to select appropriate solutions. According to Figs. 8a and 8b, the results obtained by running the research algorithm on the first model show that, through a suitable tolerance, the spatial distribution of the solutions is located quite locally on the anomaly perimeter. The algorithm can acceptably infer the anomaly boundary, which, in fact, is the location of sought cuboid source (x_0 and y_0). In this figure, the colour of each circle represents the estimated depth, while the radius size of each circle also indicates the uncertainty coefficient. As expected, and due to the natural behaviour of the potential fields at depth, lower resolution at higher depths signifies uncertainty (grey coloured circles). Histogram plots of the estimated depths confirm that the maximum distribution of solutions lies almost around the centre (Figs. 8c and 8d).

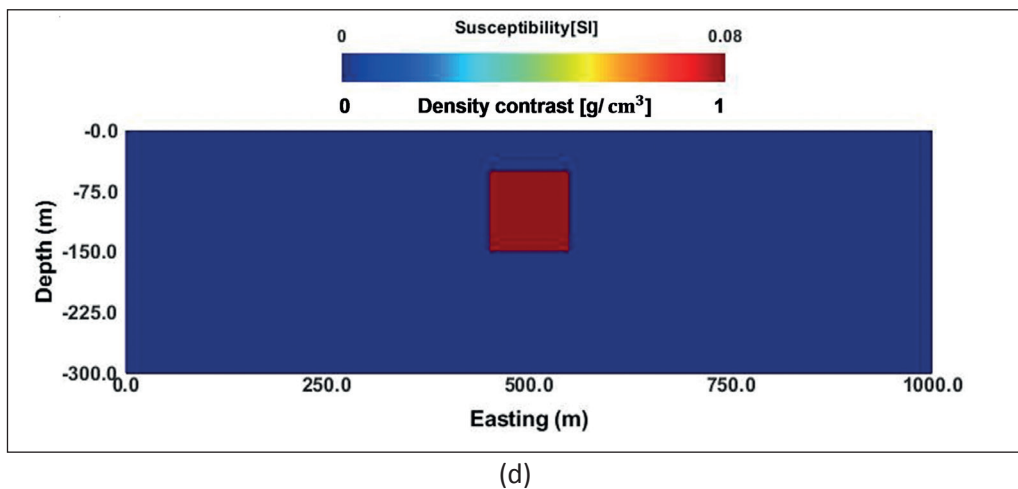
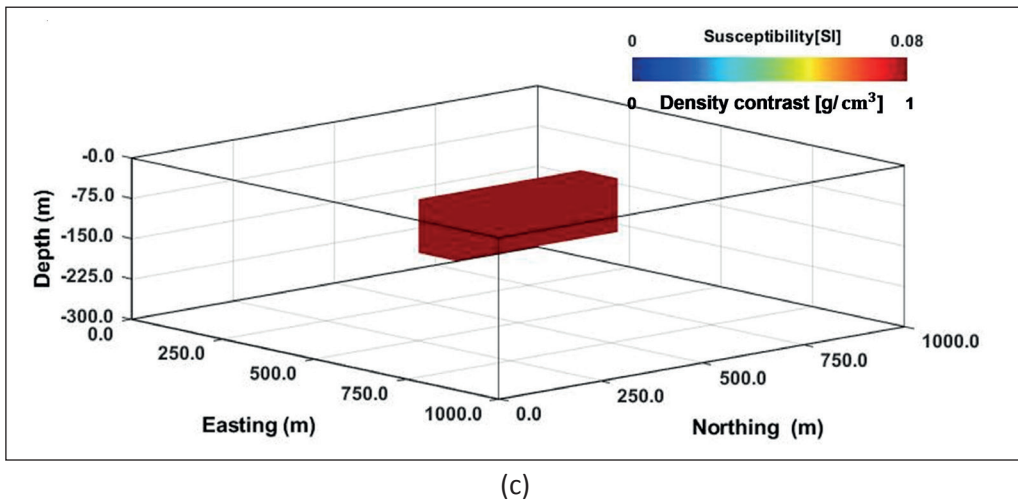
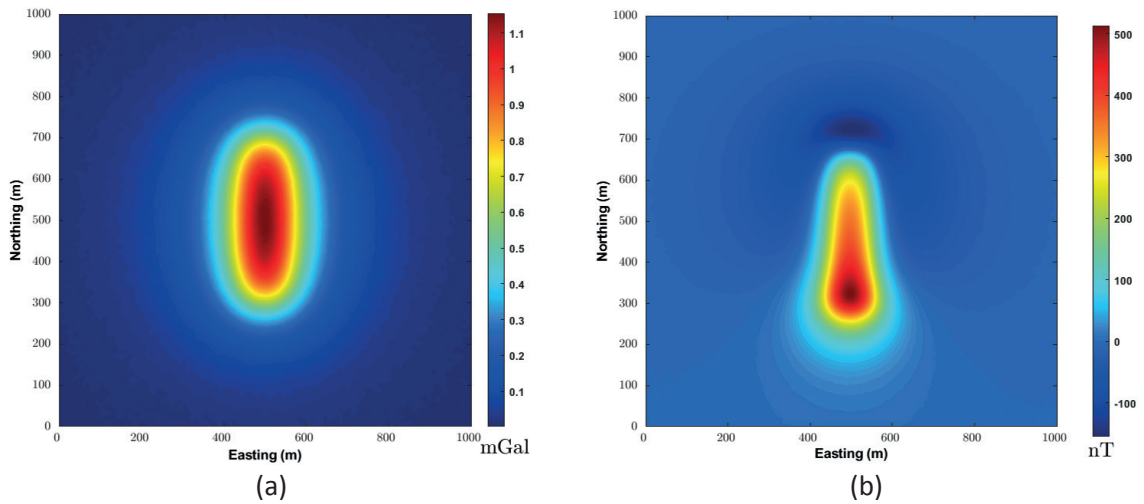


Fig. 6 - Simulation of a single source potential field anomaly: a) gravity data, b) magnetic data, c) 3D source geometry, and d) 2D cross-section at $y = 500$ m. Synthetic magnetic and gravity data are corrupted with 3% random Gaussian noise.

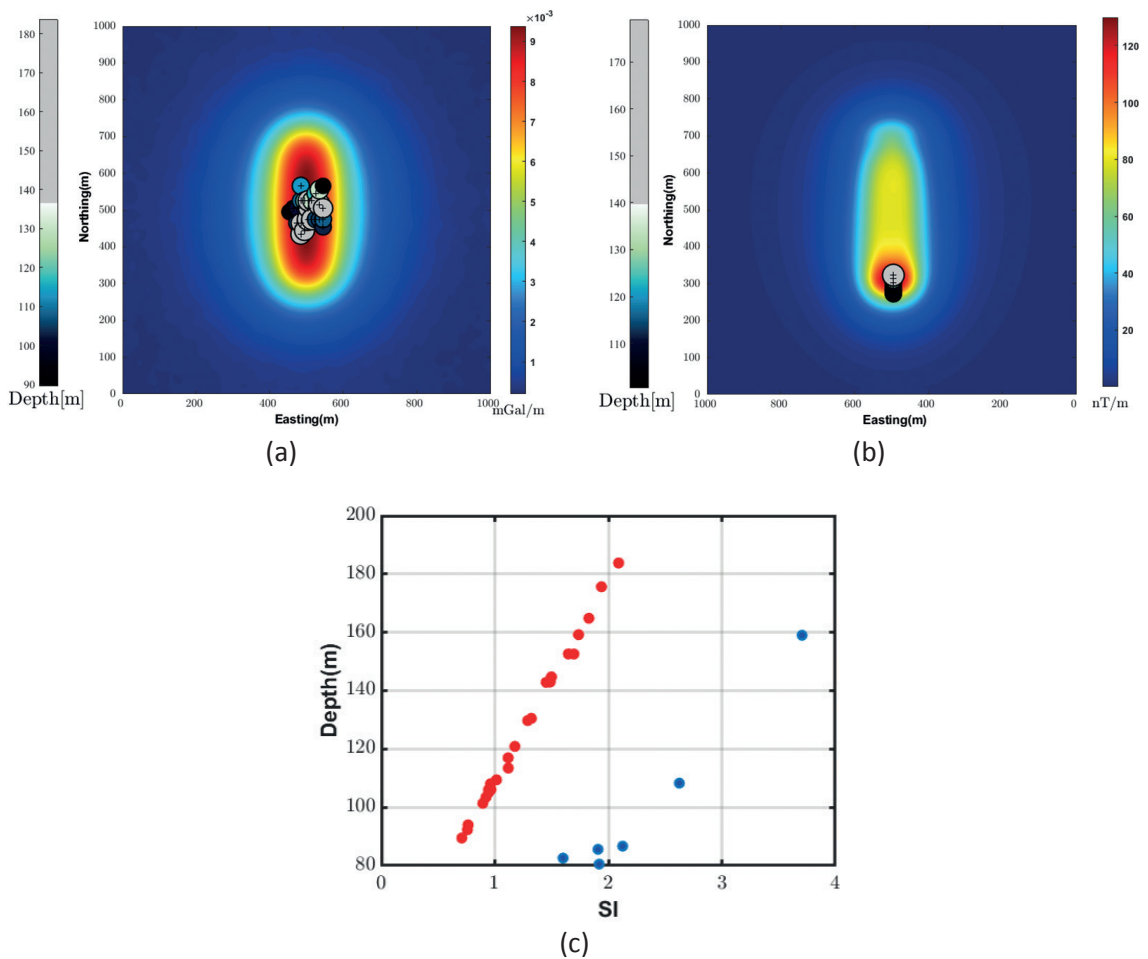


Fig. 7 - A single source analytic signal-based depth estimation over peak points: a) gravity, and b) magnetic data; and c) plot of depth versus the *SI* estimates for gravity data (red circles) and magnetic data (blue circles).

Multiple windows have acceptable depth estimates for the Euler equation, and, in different areas of the grid, different sized windows can produce acceptable estimates of the source depth considering the initial tolerance. Furthermore, within each area of the grid, the algorithm can consider optimal windows as well as minimum error values. It can be said that the algorithm successfully eliminates the dependence on choosing the same window size for all grid regions (Figs. 8e and 8f). To accurately illustrate the diffusion of the solutions, 3D images of the depths, estimated from the gravity and magnetic data, are displayed simultaneously on the cuboid model (Fig. 9). This shows that the algorithm is capable of recovering the appropriate depth distribution with acceptable accuracy, consistently with previous results.

3.2.2. Model 2

To further study the proposed method, the magnetic and gravity responses of a more complex sloping source were calculated with the magnetic susceptibility and density contrast of 0.1 *SI* and 0.3 g/cm³, respectively. Similar to the previous model, the magnetic inclination and declination

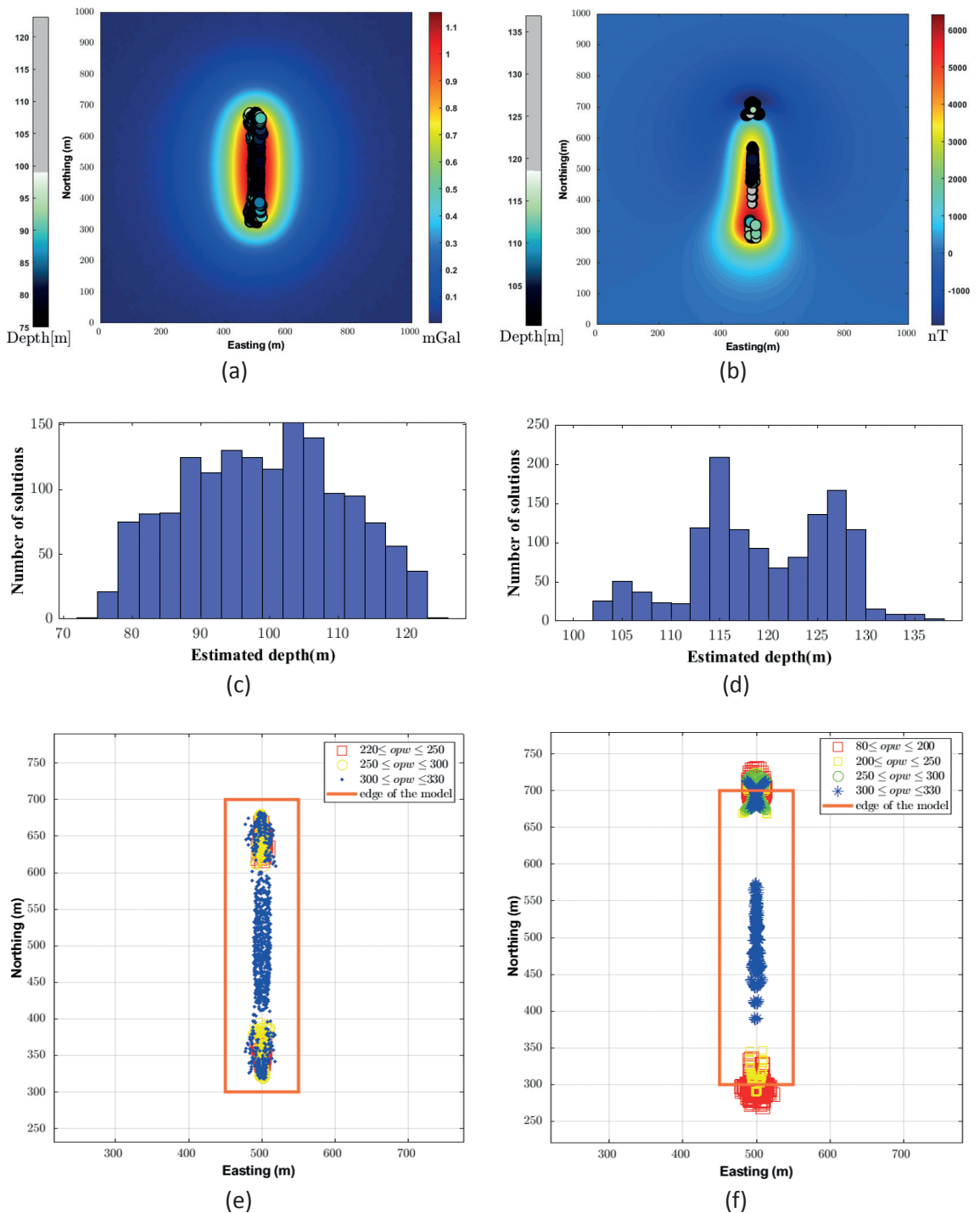


Fig. 8 - Depth estimation of a single source potential field anomaly through dynamic windows, where the left column is for gravity and the right for magnetic data, with a grid interval or spacing of 10 m. The top row illustrates depth estimation for: a) gravity, and b) magnetic data. The middle row shows the histogram plot of the depth estimation distribution for: c) gravity, and d) magnetic data. The bottom row presents the 2D plots of the dynamic optimum window size as a position function for: e) gravity, and f) magnetic data (in panels e and f, opw stands for optimum window size).

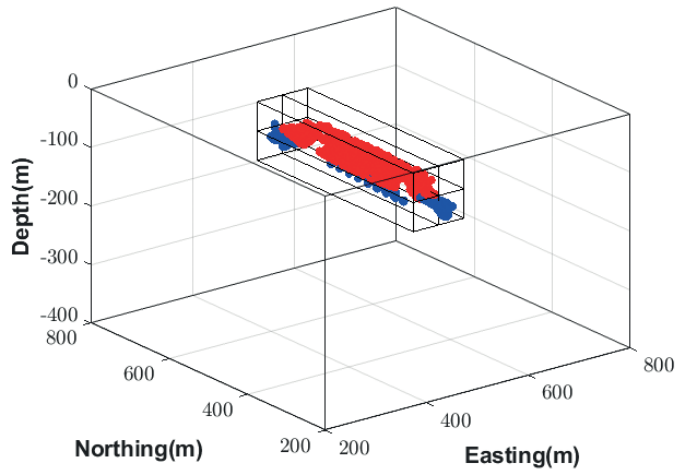


Fig. 9 - 3D visualisation of the depth estimates overlaid on the cuboid model, where red and blue circles denote the gravity and magnetic solutions, respectively.

of 55 and 3 degrees have also been considered for this model, while the general characteristics of the second model are presented in Table 5 and shown in Fig. 10.

Table 5 - Parameters assumed for the single sloping synthetic source shown in Fig. 10.

Block Size (m)	Easting from to (m)	Northing from to (m)	Z from to (m)	Slope (degree)	Density contrast (g/cm ³)	Susceptibility (SI)	Inclination (degree)	Declination (degree)
200	350	350	-50	40	0.3	0.1	55	3
400	590	700	-185					
135								

In the second scenario, for peaks above 80 nT/m and 0.013 mGal/m from magnetic and gravity data, the average *S*'s are calculated as 1.4176 and 0.4655, respectively (Fig. 11c). With the same primary conditions (initial input parameters) as the first model, the analytical signal and dynamic window-based algorithms were run. The results are shown in Figs. 11 and 12.

According to Figs. 12a and 12b, the results indicate that, through appropriate tolerance, the spatial distribution of the solutions is quite localised on the anomaly perimeter and the algorithm can acceptably infer the anomaly boundary, which constitutes the source location (x_0 and y_0). From the estimated depth charts in Figs. 12c and 12d, most of the depth solution scattering is around the centre of the synthetic gravity and magnetic sources (60 to 120 m).

Similarly to the first model, the window sizes with acceptable depth estimates have different sizes in different areas of the grid, showing that the algorithm can choose the optimal window size for each area of the mesh. Therefore, it can be affirmed that the proposed method has eliminated the dependence on a single window size for the entire measurement grid (Figs. 12e and 12f). As shown in Fig. 13, to accurately represent the diffusion of the solutions, a 3D view of the estimated depths, from the gravity and magnetic data, is displayed simultaneously on

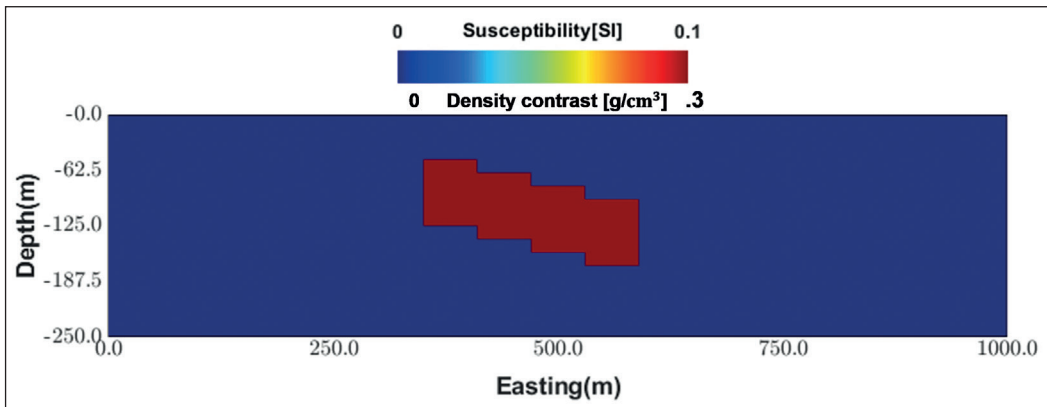
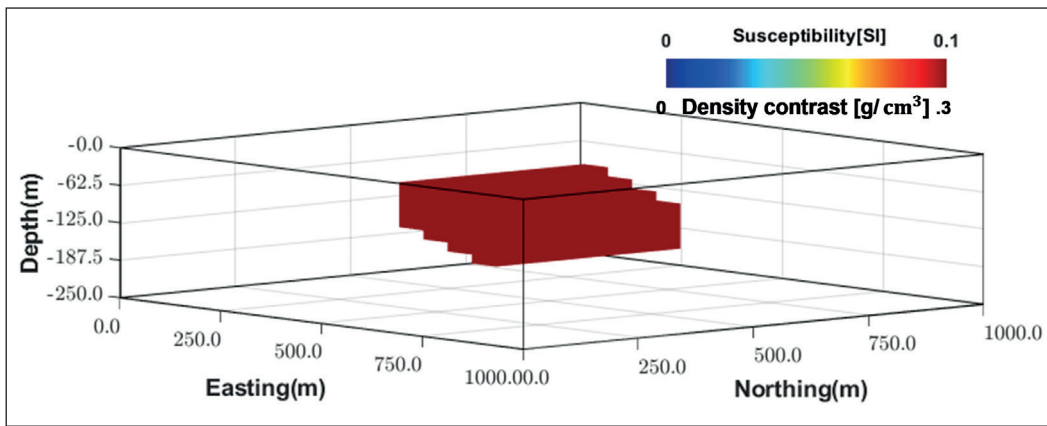
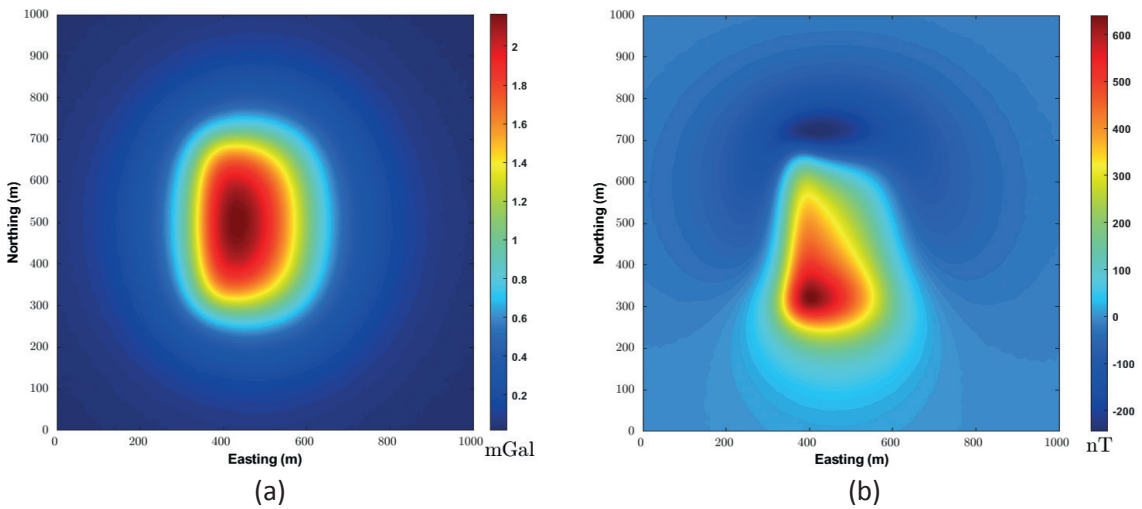


Fig. 10 - Simulation of a single sloping source potential field anomaly: a) gravity data, b) magnetic data, c) 3D source geometry, and d) 2D cross-section at $y = 500$ m. Synthetic magnetic and gravity data are corrupted with 3% random Gaussian noise.

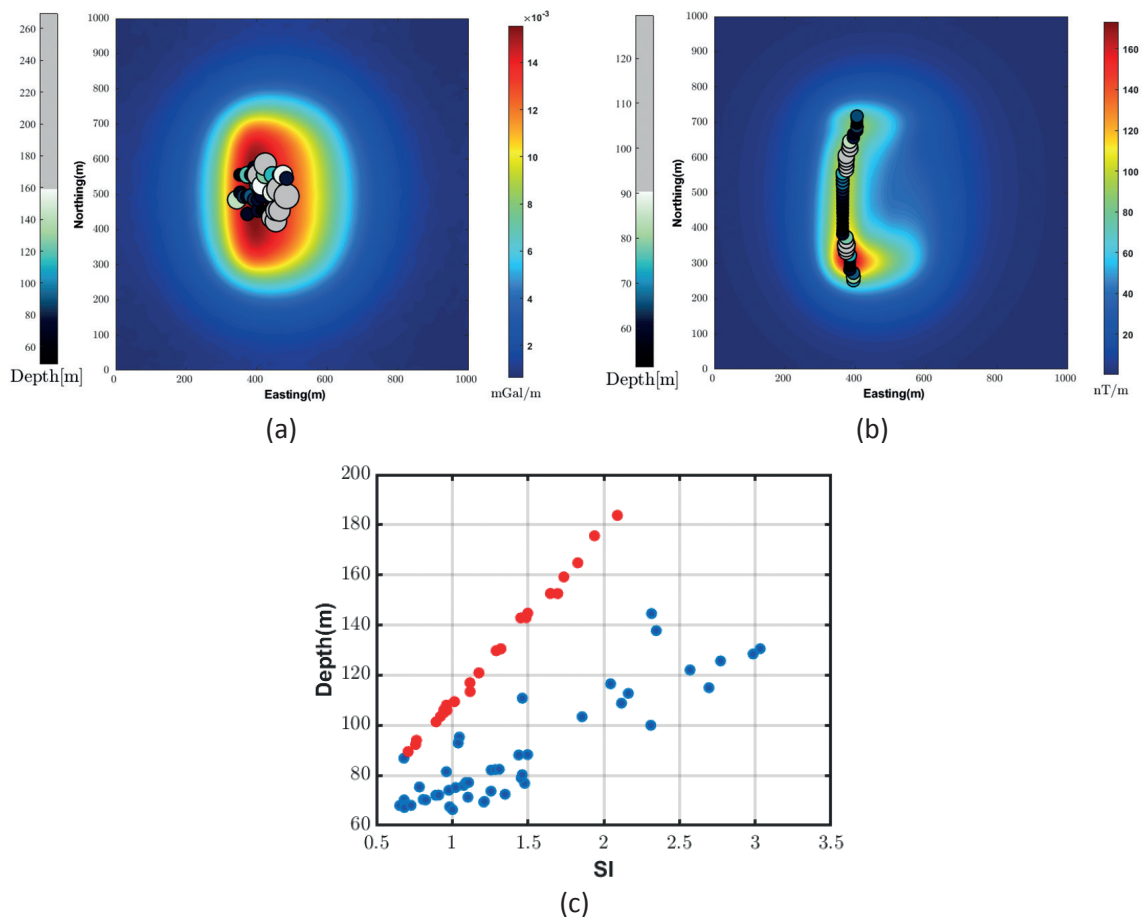


Fig. 11 - A single sloping source analytic signal-based depth estimation over peak points: a) gravity, and b) magnetic data; and c) plot of depth versus the SI estimates for gravity data (red circles) and magnetic data (blue circles).

the source, revealing that the algorithm is fully capable of recovering the appropriate depth distribution along the sloping source.

Model 3 - To carry out a comprehensive study of the method presented in this paper, the magnetic and gravity responses of a more complex model were examined. The third synthetic model is the combination of a sloping source with a magnetic susceptibility of 0.05 (SI) and density contrast of 0.75 g/cm^3 , placed next to a cuboid with a 0.1 magnetic susceptibility (SI) and 1.5 g/cm^3 density contrast (Fig. 14). Similarly to the previous models, the inclination and declination angles of the Earth’s magnetic field are 55 and 3 degrees, respectively. Table 6 summarises the geometrical and the physical properties of the third synthetic model.

In the third synthetic model, for peaks above 1.5 nT/m and 0.006 mGal/m from magnetic and gravity data, the average SI s are calculated as 1.3218 and 0.4523, respectively (Fig. 15). The minimum window size was considered as three times greater than the cell size, so as to perform the calculations with a 90% overlap. The maximum value for the window size is, also, 33 times greater than the cell size for the magnetic and gravity data. The initial 3% (ϵ) tolerance condition was also applied for the selection of the final solutions (Fig. 16).

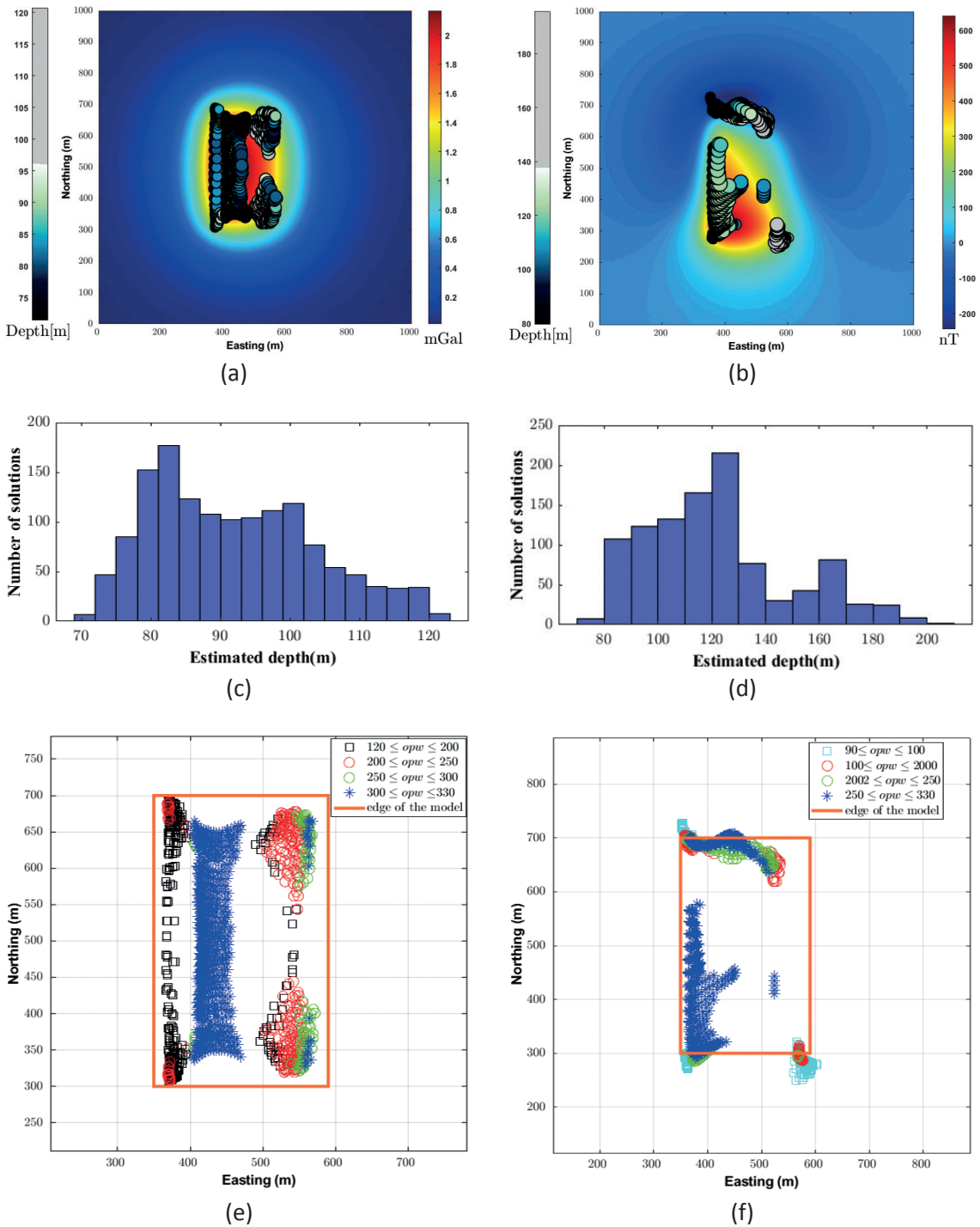


Fig. 12 - Depth estimation of a single sloping source potential field anomaly through dynamic windows, where the left column is for gravity and the right for magnetic data, with a grid interval or spacing of 10 m. The top row illustrates depth estimation for: a) gravity, and b) magnetic data. The middle row shows the histogram plot of the depth estimation distribution for: c) gravity and d) magnetic data. The bottom row presents the 2D plots of the dynamic optimum window size as a position function for: e) gravity, and f) magnetic data (in panels e and f, opw stands for optimum window size).

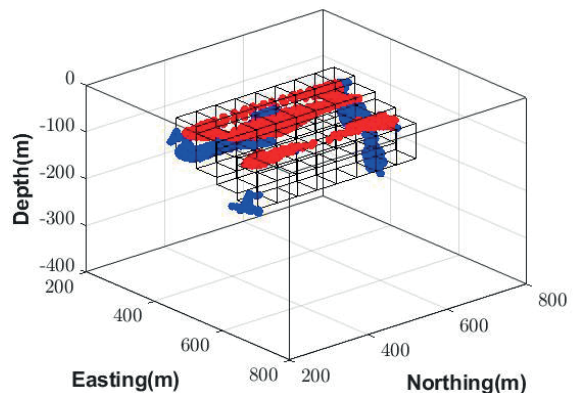
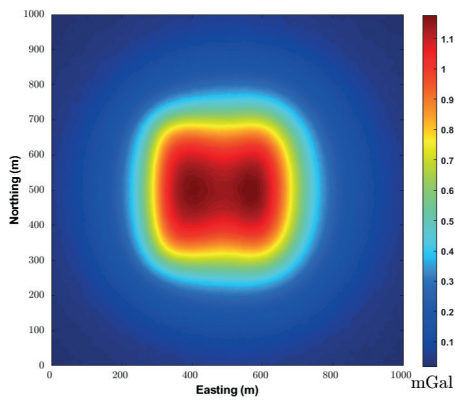
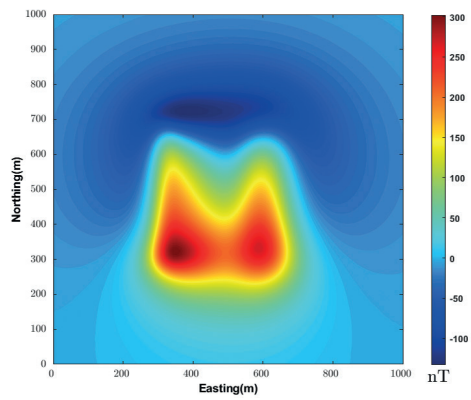


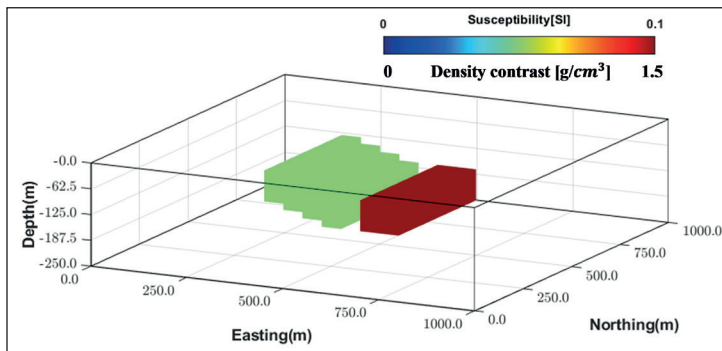
Fig. 13 - 3D visualisation of depth estimates overlaid on a single sloping source, where red and blue circles denote the gravity and magnetic solutions, respectively.



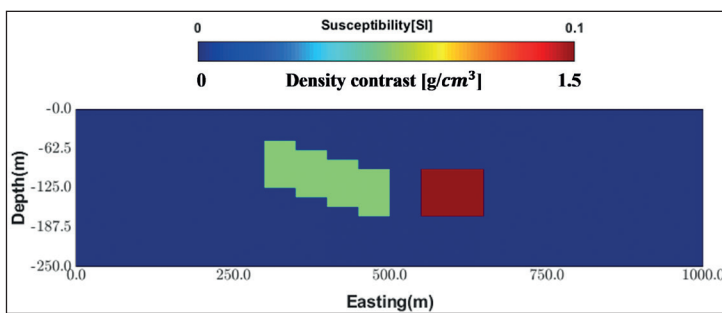
(a)



(b)



(c)



(d)

Fig. 14 - A multi-source potential field anomaly simulation: a) gravity data, b) magnetic data, c) 3D source geometry, and d) 2D cross-section at $y = 500$ m. Synthetic magnetic and gravity data are corrupted with 3% random Gaussian noise.

Table 6 - Parameters assumed for the synthetic multi-source model shown in Fig. 14.

Block Size (m)	Easting from to (m)	Northing from to (m)	Z from to (m)	Slope (degree)	Density contrast (g/cm ³)	Susceptibility (SI)	Inclination (degree)	Declination (degree)
250 400 135	300 500	300 700	-50 -185	28.5	0.75	0.05	55	3
100 400 70	550 650	300 700	- 115 -185	-	1.5	0.1	55	3

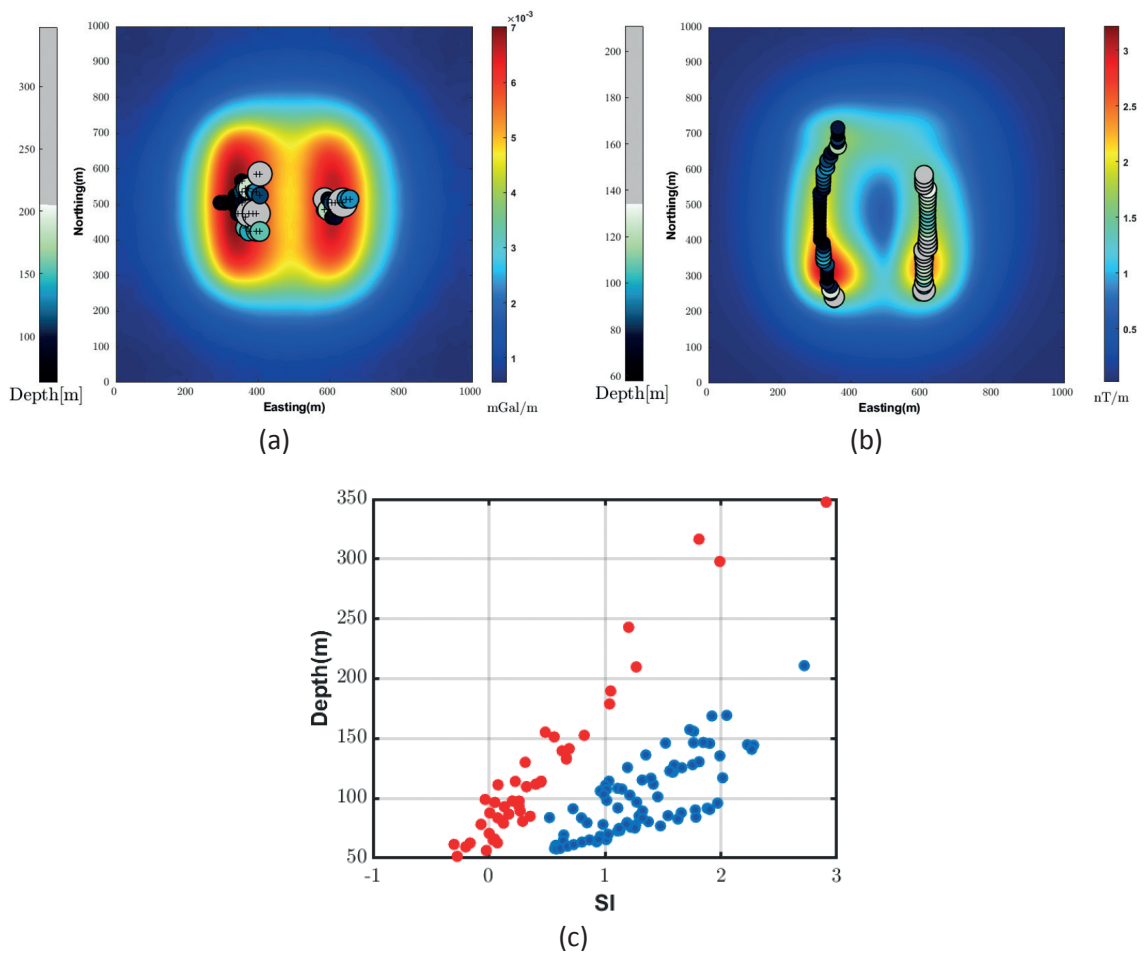


Fig. 15 - A multi-source analytic signal-based depth estimation over peak points: a) gravity, and b) magnetic data; and c) plot of depth versus the *SI* estimates for gravity data (red circles), and magnetic data (blue circles).

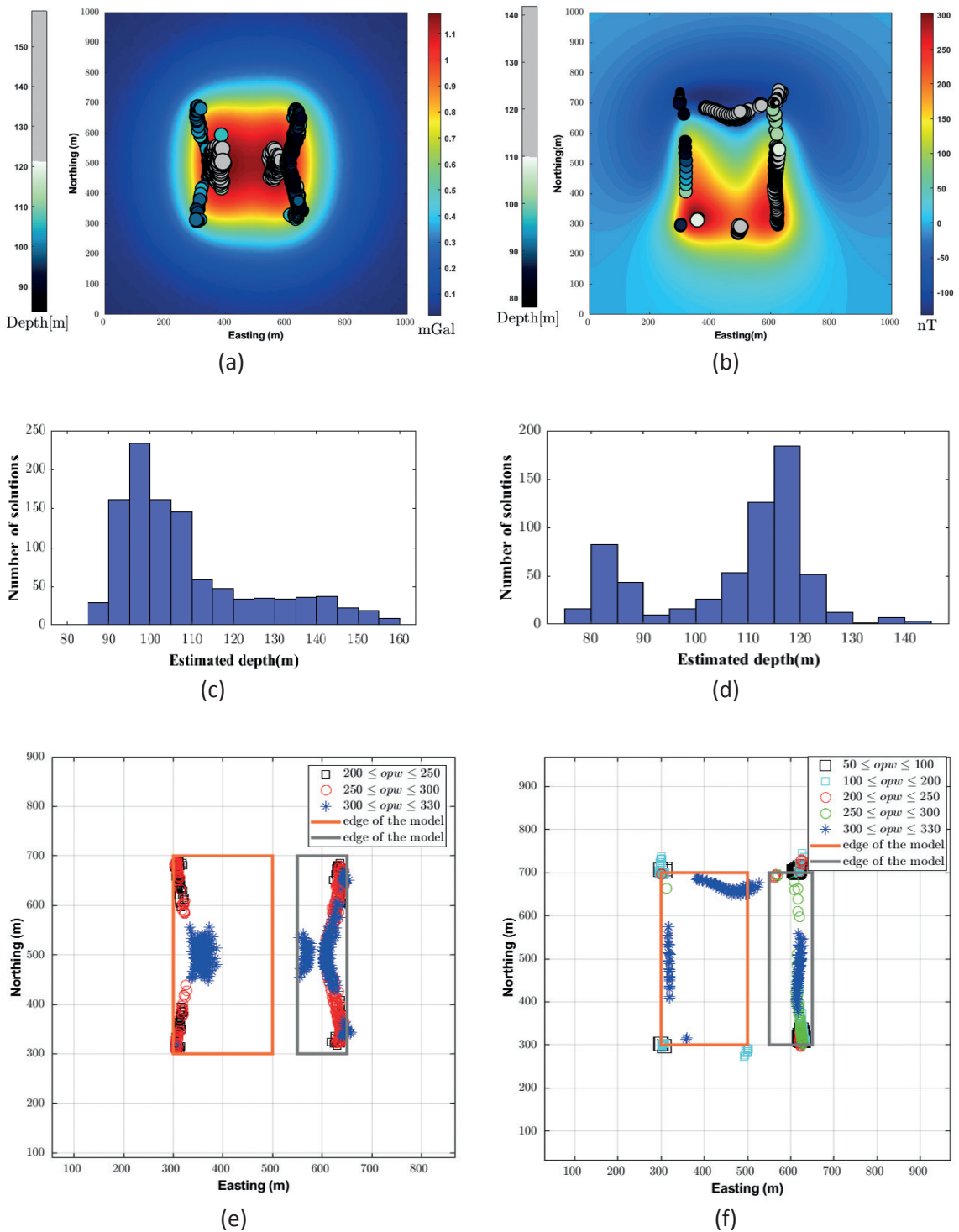


Fig. 16 - Depth estimation of a multi-source potential field anomaly through dynamic windows, where the left column is for gravity and the right for magnetic data with a grid interval, or spacing, of 10 m. The top row illustrates depth estimation for: a) gravity, and b) magnetic data. The middle row shows the histogram plot of the depth estimation distribution for: c) gravity, and d) magnetic data. The bottom row presents the 2D plots of the dynamic optimum window size as a position function for: e) gravity and f) magnetic data (opw stands for optimum window size).

According to Figs. 16a and 16b, the results indicate that the algorithm presented can, to an acceptable level, recover the appropriate depth diffusion along the sloping potential source next to the cuboid model. The histogram plots, also, indicate that the maximum depth scattering is, quite significantly, between 90 and 120 m for both the magnetic and gravity observations (Figs. 16c and 16d). Similarly to the previous models, the window sizes with acceptable depth estimates for the Euler equation have different dimensions in different areas of the observation grid, showing that the proposed method has been fairly well able to eliminate the dependency on choosing the same size for all grid areas (Figs. 16e and 16f). As previously mentioned, the algorithm actually uses a set of window sizes for the entire mesh, and the acceptable depth solutions and window sizes are calculated simultaneously. The importance of the algorithm usability is especially significant in the third synthetic model, where multiple sources are considered with different dimensions and depths. In such cases, by using the standard Euler method, the interpreter must use different window sizes multiple times to find the appropriate fixed window size for all regions of the grid. Due to the geological complexity of the subsurface structures, many different sources and anomalies may be in close proximity, and this algorithm helps the interpreter to obtain depth and window sizes with greater ease.

Similarly to previous synthetic models, to properly observe the solutions on the potential sources, Fig. 17 depicts the magnetic and gravity Euler depth solutions superimposed on the 3D transparent volumes of the third synthetic model. Clearly, the algorithm can accurately restore the depth diffusion of the complex synthetic model. Therefore, in such cases, using a fixed window size for all the grid points can be quite difficult, or may increase errors.

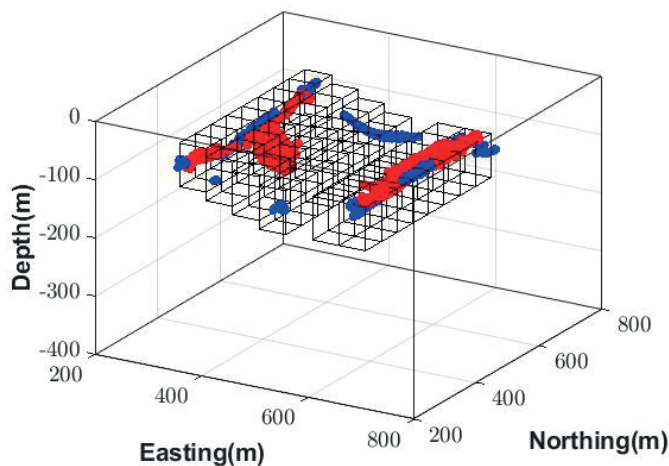


Fig. 17 - 3D visualisation of depth estimates overlaid on the multi-source model, where red and blue circles denote the gravity and magnetic solutions, respectively.

3.3. Comparison of dynamic and fixed window depth estimation

To compare the results of dynamic Euler obtained with the fixed window method, depth estimation is performed with fixed windows of different sizes for the three synthetic models. To avoid excessive repetition, the results are presented for six different sizes. Except for the window size, all other input values are considered identical for both algorithms. Figs. 18 to 20 present the following 3D gravity and magnetic field results.

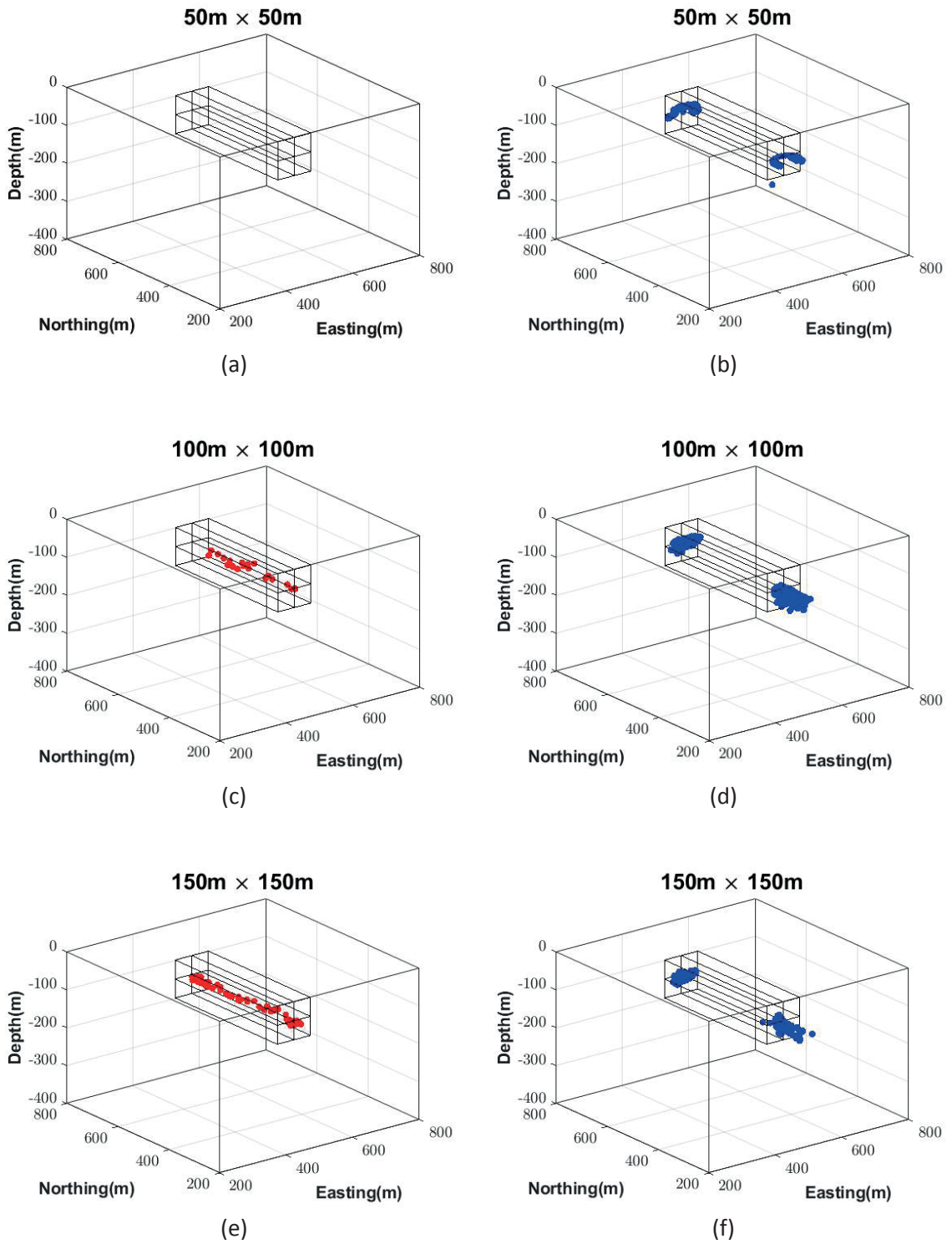
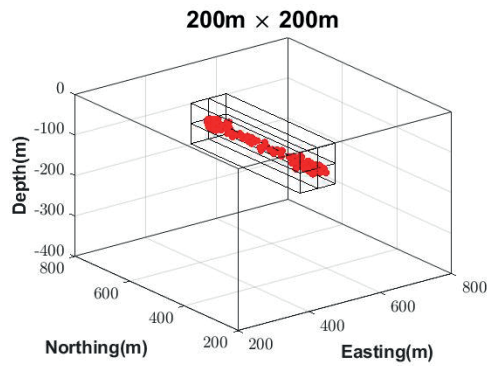
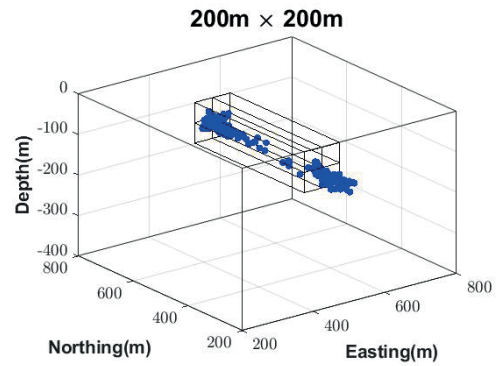


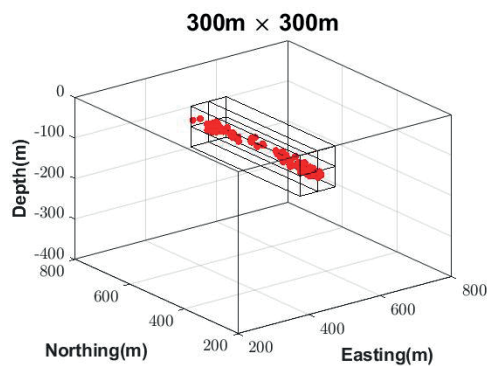
Fig. 18 - Comparison between the dynamic Euler depth estimation and the different fixed window sizes (window sizes are given above the figures) for the first synthetic model (gravity data on the left side and magnetic data on the right), where the tolerance is 3% of the depth estimation, and SI is 2.3146 and 1.2617 for magnetic and gravity, respectively.



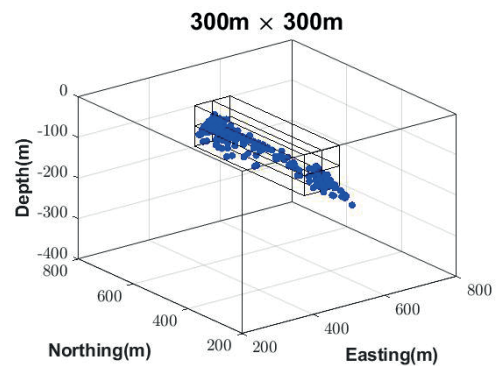
(g)



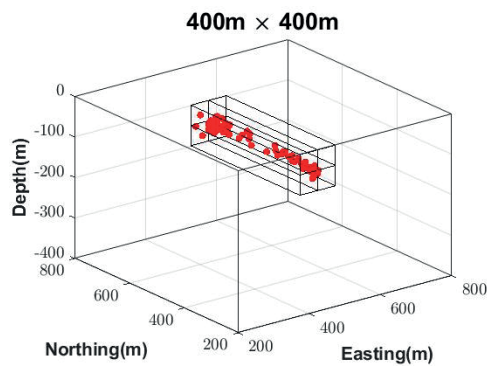
(h)



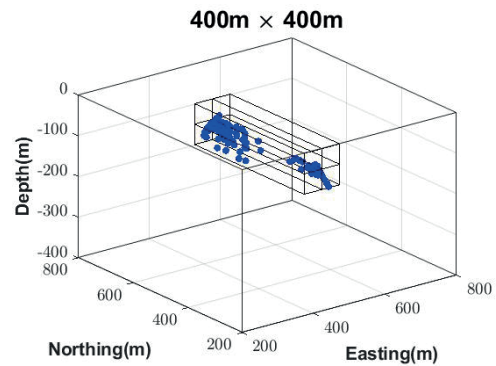
(i)



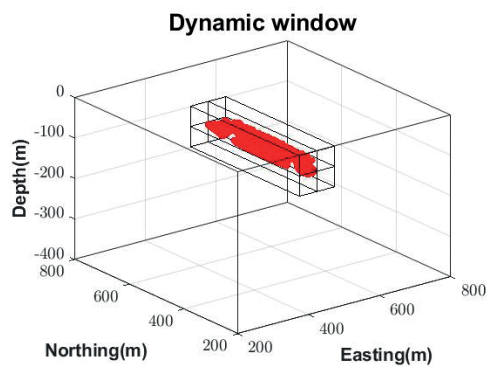
(j)



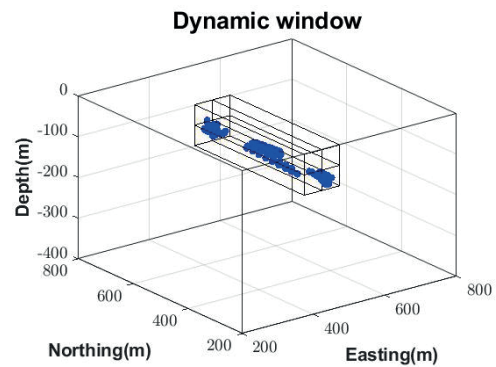
(k)



(l)



(m)



(n)

Fig. 18 - continued.

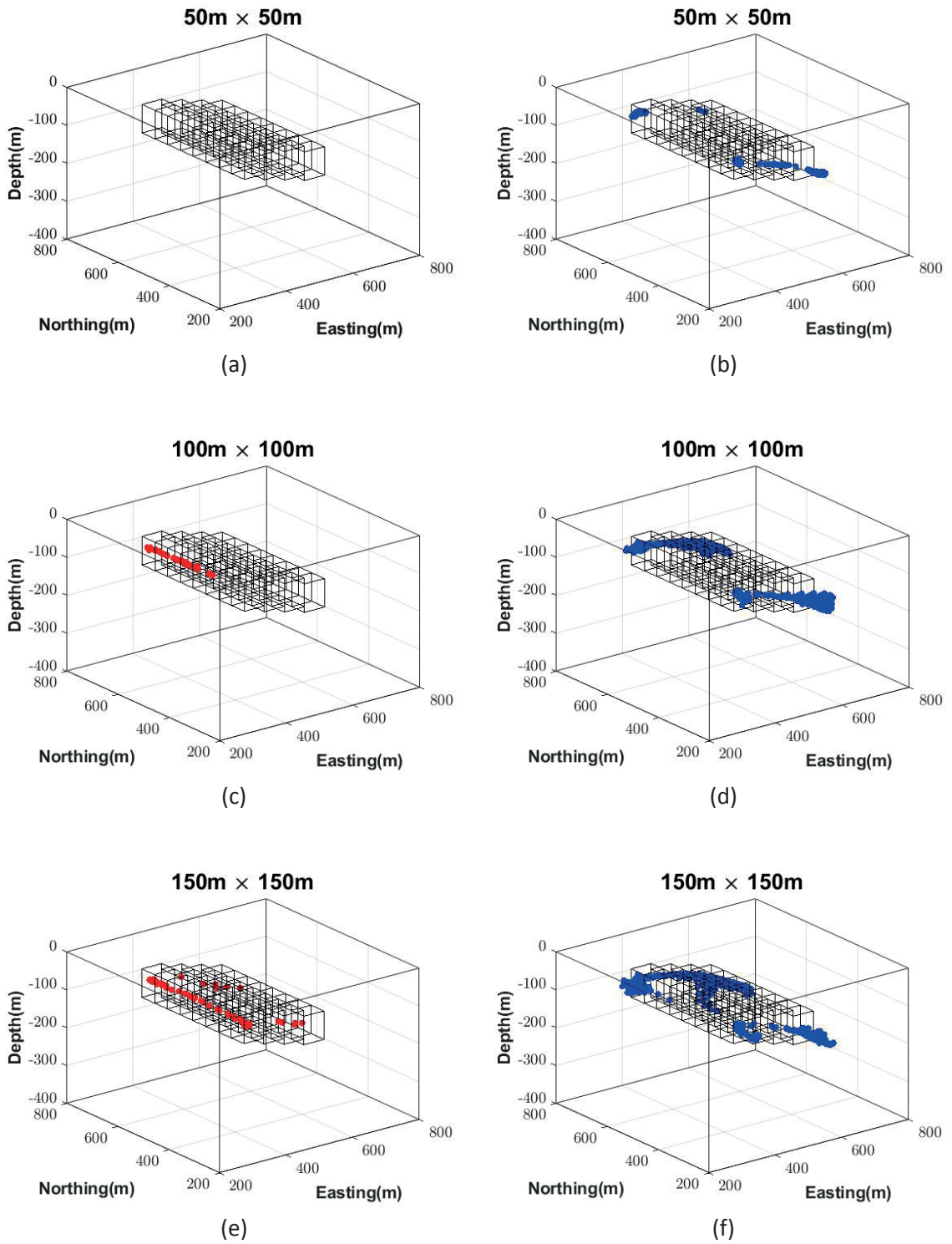


Fig. 19 - Comparison between the dynamic Euler depth estimation and the different fixed window sizes (window sizes are given above the figures) for the second synthetic model (gravity data on the left side and magnetic data on the right), where the tolerance is 3% of the depth estimation, and S_I is 1.4176 and 0.4655 for magnetic and gravity, respectively.

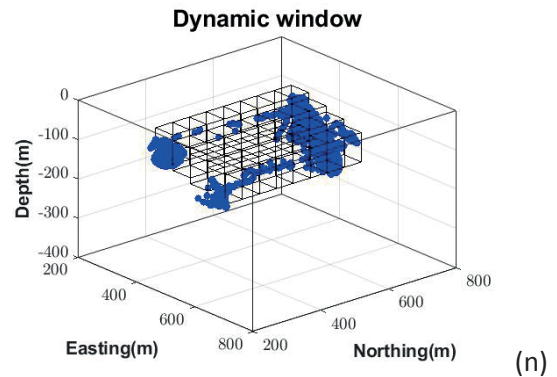
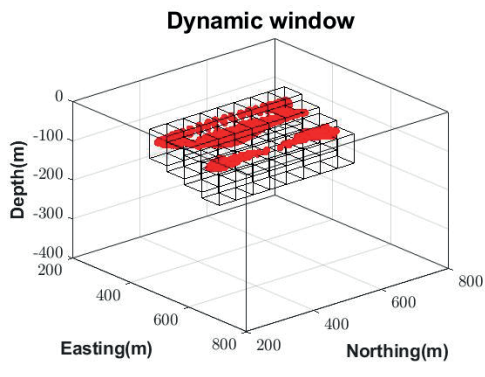
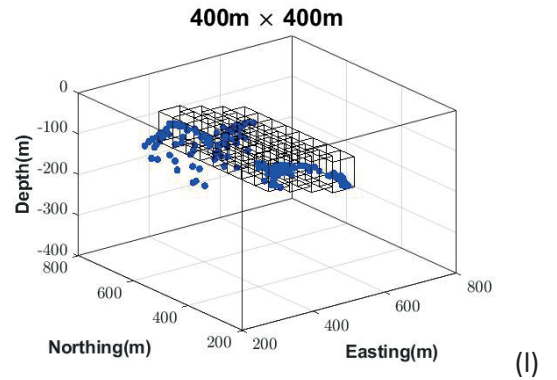
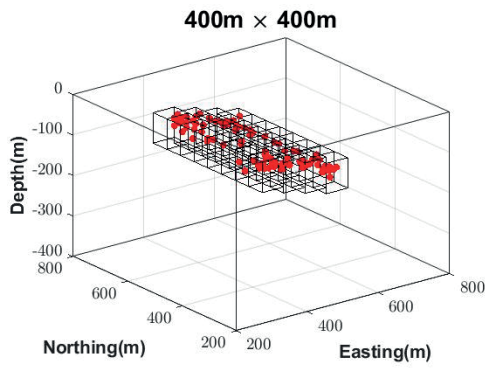
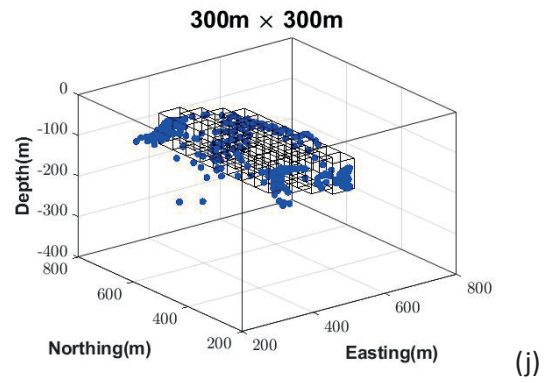
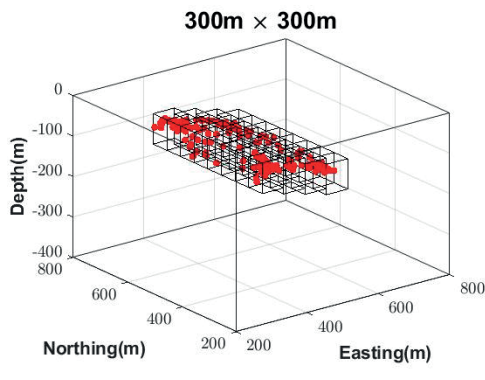
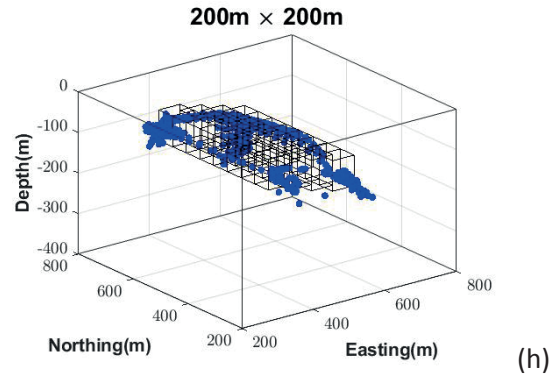
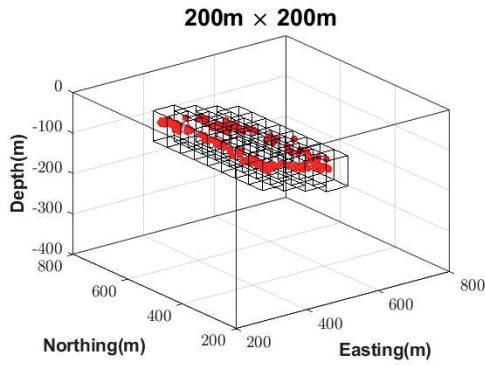


Fig. 19 - continued.

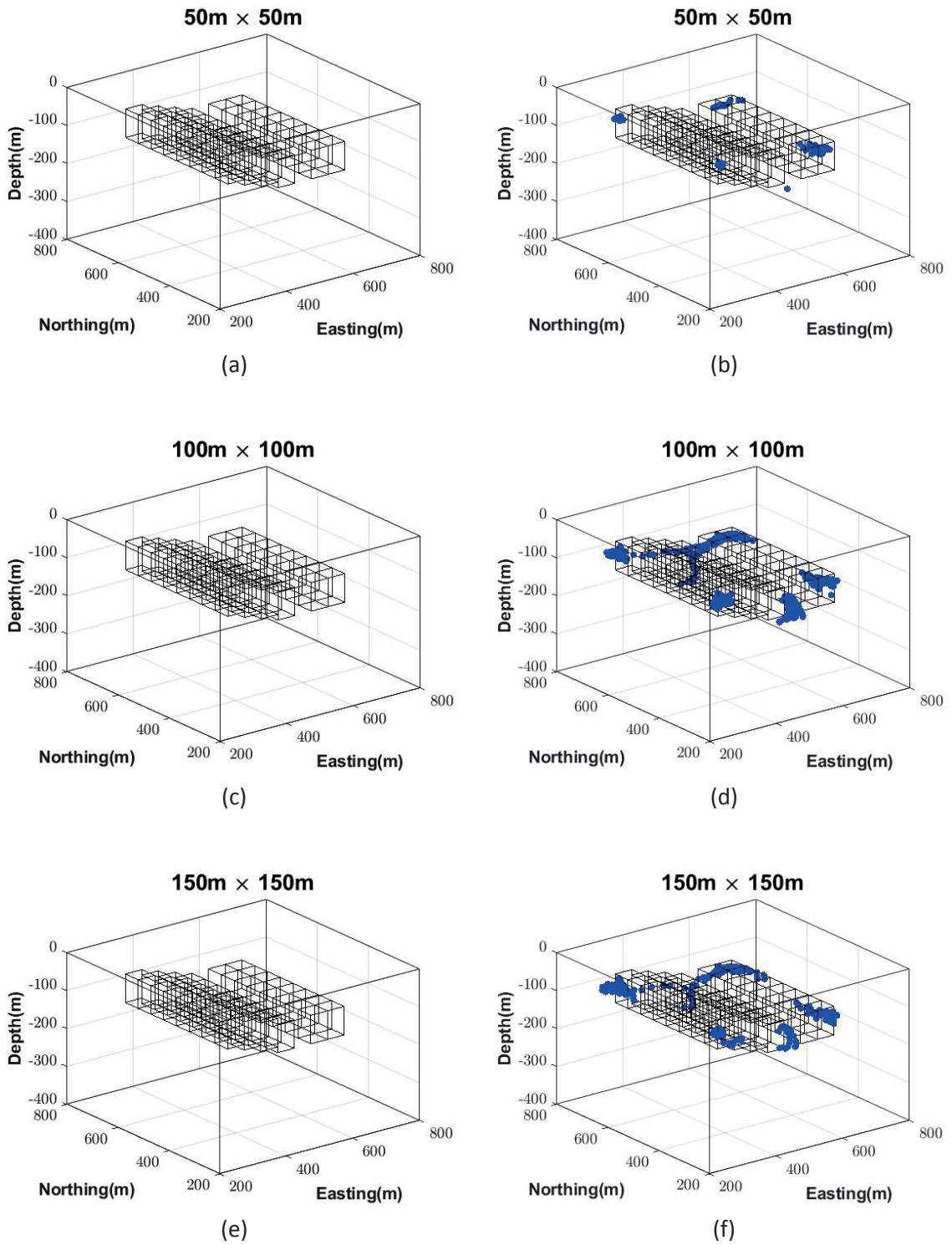
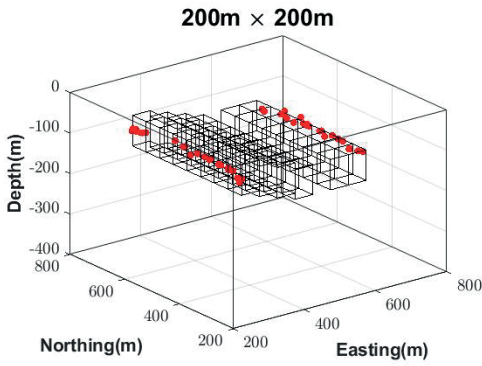
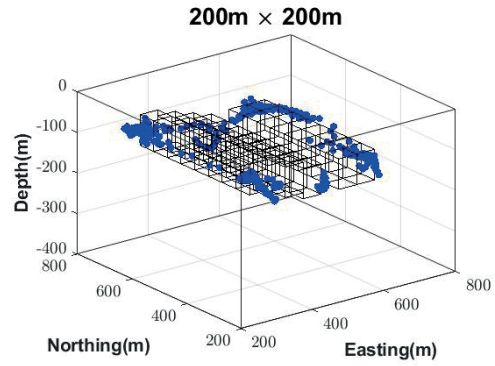


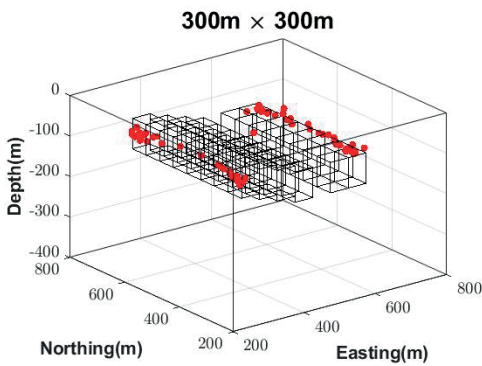
Fig. 20 - Comparison between the dynamic Euler depth estimation and the different fixed window sizes (window sizes are given above the figures) for the third model (gravity data on the left side and magnetic data on the right), where the tolerance is 3% of the depth estimation, and S_I is 1.3218 and 0.4523 for magnetic and gravity, respectively.



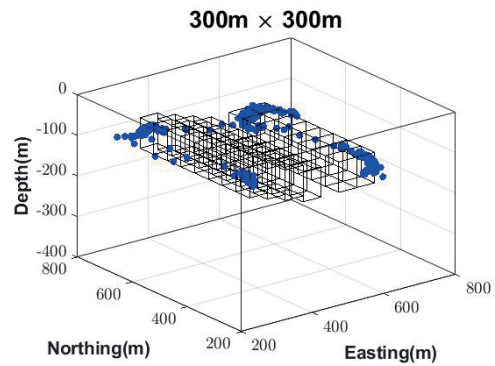
(g)



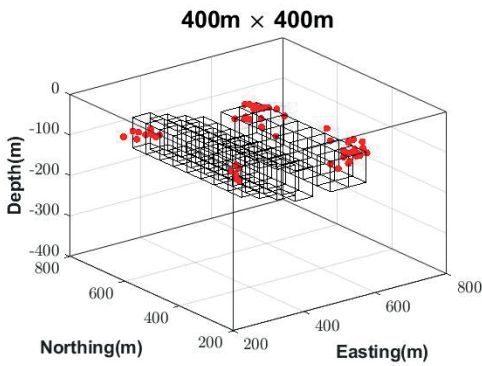
(h)



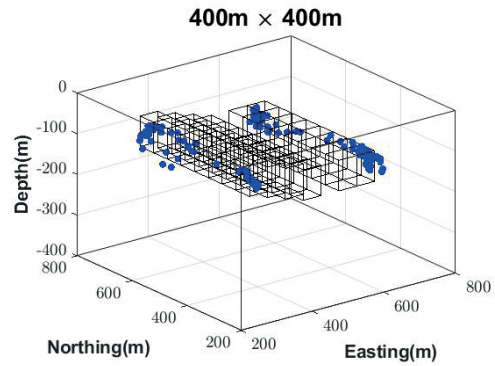
(i)



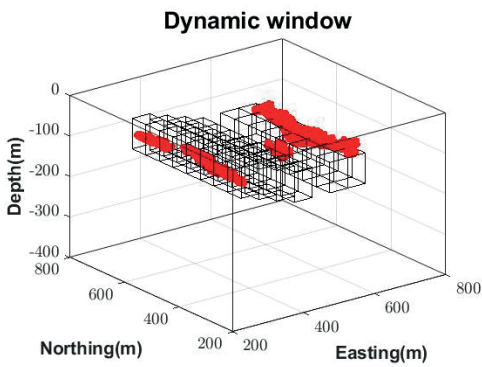
(j)



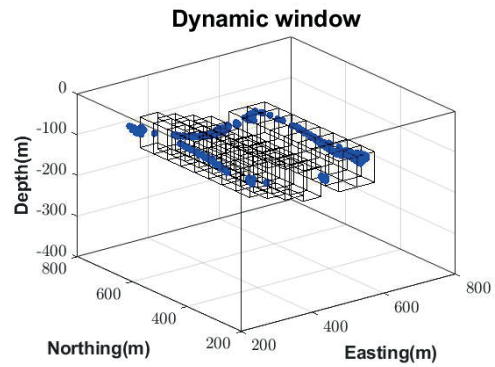
(k)



(l)



(m)



(n)

Fig. 20 - continued.

A review of the results would indicate that: 1) the standard Euler equation with a fixed window can estimate the depth solutions within the source range, while many solutions are beyond the target locations, and the number of the obtained solutions far from the targets are high compared to the dynamic approach; 2) certain window sizes will provide better responses; 3) each window will return a different response, while multiple window sizes will provide nearly identical solutions. As a result, the dynamic Euler results consist of the best solutions of a set of Euler solutions to fixed windows of many sizes, and, conversely, the dynamic approach can improve the results to a certain level, compared to the fixed windows. Next, the results of the three ensemble models of the above-mentioned study were compared separately.

The analysis of the Euler results with fixed windows, as shown in Fig. 18 for the first model, reveals that the gravity estimations, for small window sizes (e.g. 50×50 m²), are inaccurate and unreliable. As can be inferred from Figs. 19 and 20, the same is true for the second and third models as well. Another important and obvious issue, especially for the magnetic sources, is that the Euler solution for small windows manifests only at the source boundary points, and the distribution of the solutions, over the causative source, is inappropriate. The increase of the window size to a certain extent, clearly, caused some of the solutions to be located at a horizontal distance from the source. In contrast, the inspection of the dynamic Euler results, for the horizontal cuboid model (Fig. 18), demonstrates that the depth solution lies almost above the source centre. Additionally, the number of solutions, located far from or outside the source, is significantly smaller, which may indicate a suitable improvement of the proposed algorithm.

More complicated than the first model, the examination of the results of the second and third models also shows that, for the gravity anomaly sources, the histogram of the dynamic window method is in better agreement with the results of the fixed window solution with 50×50 m² and 100×100 m² for both synthetic models mentioned. In addition, the number of outlier solutions is much smaller in the dynamic Euler method. The interpreter may need to repeat the calculations for multiple window sizes to obtain more accurate solutions. Worth mentioning is that this process may take longer and may, also, increase possible personal errors by the interpreter. Overall, it can be said that the results have been accurately improved by the proposed algorithm.

4. Geological setting of the studied region

In terms of geological structure division, the study area is located in the Urmia-Dokhtar magmatic belt (Fig. 21a). With a length of 1,600 km, this structural zone extends from the NW to the SE of Iran and consists of felsic igneous rocks and intermediate felsic pyroclastic rocks from the Cretaceous to the Eocene with granitoid intrusions of the Eocene-Oligocene to the Miocene. Heretofore, more than 200 mineral deposits have been identified in the Urmia-Dokhtar volcanic region, and, apparently, these mineralogical events are related to the structure of the area, especially the main faults (e.g. Shafiei, 2010; Agard *et al.*, 2011). One of the major faults in this area, with a substantially significant impact on mineralisation, is the Dehshir fault, with a strike of N150° to N160°, a length of approximately 380 km and a crushed fault zone from 2 to 3 km wide. This fault, with a right-slip mechanism, has caused a displacement of about 65 km in the Urmia-Dokhtar arc (Meyer *et al.*, 2006).

Fig. 21b shows the geological map of the study area taken from the 1:100,000-scale map of Kafeh-Taghestan. The study area is located in a plain, leading to Kafeh-Taghestan from the west, with elevations with a NW-SE direction to the north. Starting from the south of Naean and continuing

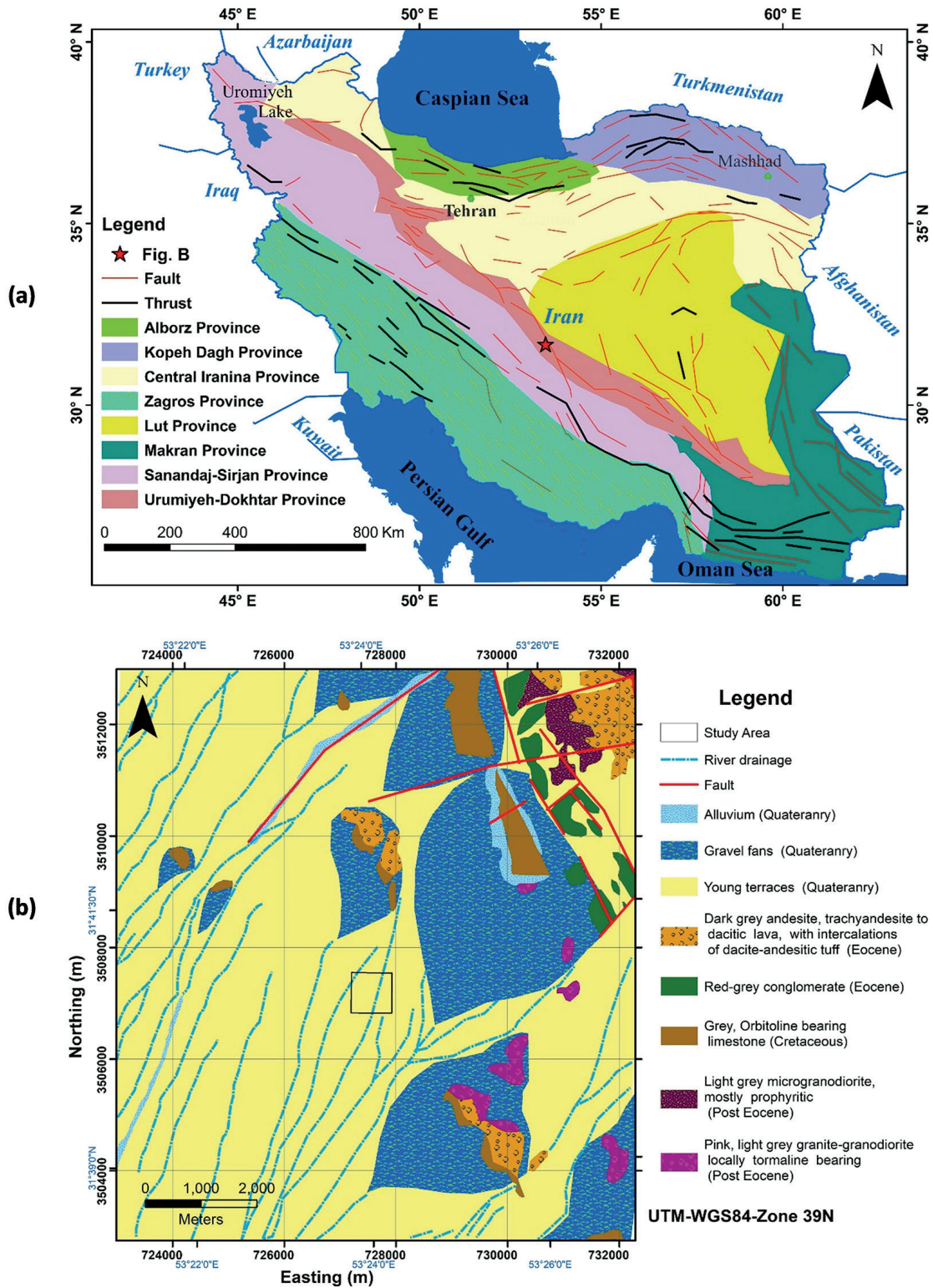


Fig. 21 - Geological description of the studied area: a) location of the study area on the structural geology map of Iran, and b) enlarged view near the region of the study area produced from a 1:100,000-scale map of the Kafeh-Taghestan (Ghahamghash and Mohammadiha, 2005).

to the east of Dehshir, this plain area features a large number of lenses with iron mineralisation (usually magnetite), most of which formed adjacent to the Cretaceous and Permian carbonate units, and only some next to intermediate dykes. Thus, due to the uneven slope of the sedimentary units, they are, apparently, in connection with the magmatic activities in the region. Possible iron mineralisation, existing beneath the Quaternary sedimentary units in the absence of outcrops, is the main subject of this study, where prospective field studies are widely used in the exploration of magnetite iron mineralisation, beneath alluvial layers (Ghalmghash and Mohammadiha, 2005).

According to geological reports and previous studies, Shavaz iron mineralisation was formed in the sub-fractures of the Dehshir Fault. As shown in Fig. 21b, and based on field investigation, the geophysical survey area of this study is covered by alluvium, and in some places andesite and diabase exposures also appear. Metamorphic rocks, such as siliceous shale and green schist, were also observed in the study area. Sequences of shale carbonate rocks (dolomite) and igneous rocks (andesite) are visible near the mineralisation occurrences. Iron mineralisation mainly consists of hematite and a lower proportion of magnetite, originating from the boundary of the andesitic mass with tuff (Abedi, 2020).

5. Potential field geophysical survey for iron-bearing exploration

In this section, the algorithm is run on a real data set of magnetic and gravity fields in the Shavaz region. The potential field geophysical survey was employed along the 18 N-S profiles, with distance varying from 50 to 100 m. The stations are deployed at a distance ranging from 25 to 50 m. A 500×600 m² size grid is cropped within the whole survey area to indicate the traces of iron occurrences. Fig. 22 represents the total field magnetic map and Bouguer gravity map, gridded with a 10-metre cell size, and applying a minimum curvature method through the Geosoft software.

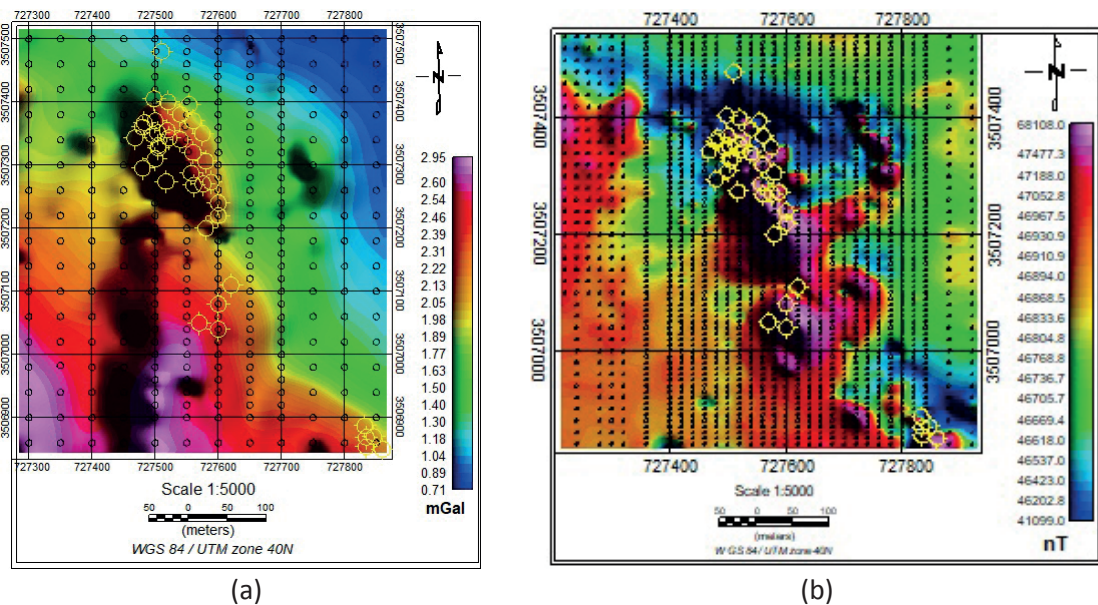


Fig. 22 - The potential field data maps: a) Bouguer gravity data, and b) total field magnetic data, where black points indicate the survey stations and the yellow symbol indicates the exploratory drillings.

Before the data is fed into the proposed algorithm, a series of corrections needs to be made to prepare the data for the format most suitable for depth estimation. This is carried out by improving the performance and accurately evaluating the results. The Earth’s magnetic field has an intensity of 46,500 nT, with inclination and declination angles of 49 and 3 degrees, respectively. It is clear that the main iron target source has an extension following the NNW-SSE trend, indicating the impact of the Dehshir-Baft Fault on the iron trap (Abedi, 2020). In the next step, to obtain the residual map, the influence of the Earth’s magnetic field strength was removed from the magnetic data through the elimination of the International Geomagnetic Reference Field (IGRF) values (Fig. 23). The first-order regional trend was, then, removed from the potential field observation using a polynomial fitting method (Fig. 24).

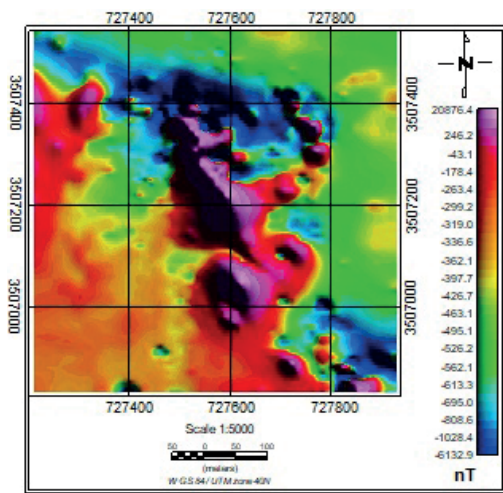
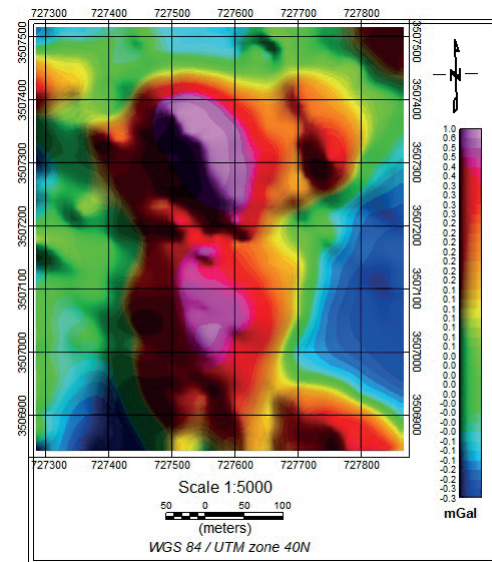
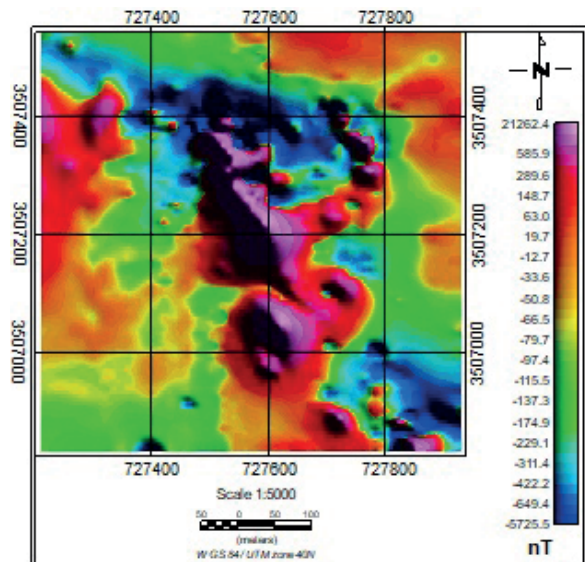


Fig. 23 - The residual total field magnetic data after removing an IGRF effect.



(a)



(b)

Fig. 24 - The residual maps of potential field data: a) gravity data, and b) magnetic data after removing a first-order regional trend.

In the northern part of the study area, the maximum magnetic anomaly value is 21,262.4 nT, whereas the gravity anomaly value is 1 mGal, which is a suitable geophysical signature for a dense and magnetised subsurface mass. To reduce the influence of surface noise, the magnetic and gravity data continued upwards to an altitude of 20 m (Fig. 25).

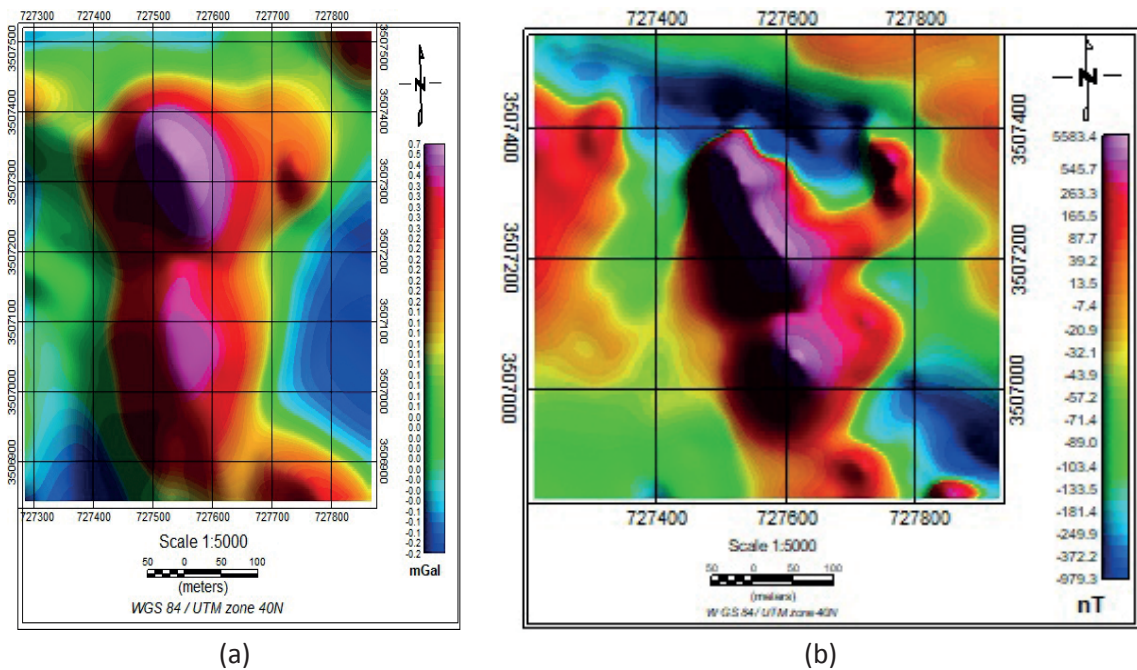


Fig. 25 – Twenty-metre upward continuation of potential field data applied to the residual maps: a) gravity data, and b) magnetic data.

In the next step, to better define the anomaly boundaries, an analytical signal filter is performed on the data. Consequently, the black polygon region was selected for further interpretation, and to implement the dynamic window-based Euler deconvolution method (Fig. 26).

Similarly to the synthetic approach adopted, the average SIs were calculated with the Salem and Ravat (2003) method, i.e. through the analytic signal process of magnetic and gravity data, equal to 1.9 and 0.9, respectively (Figs. 27a and 27b). As previously mentioned, this method also provides depth estimation as well as the SI (Fig. 27c). The maximum depth solution ranges from 50 to 100 m for magnetic and gravity data, respectively.

Here following, the dynamic algorithm is run on the Shavaz data sets, which take into account an initial tolerance of 5% for magnetic and gravity data, and a minimum and maximum window size that is 3 to 13 times the size of the grid spacing. Figs. 28a and 28b show the depth solutions of the proposed algorithm on the magnetic and gravity field maps. Results for the northern part of the grid show a depth ranging from 49 to 60 m from the gravity data and, also, a depth from 36 to 70 m from the magnetic data. These values are also consistent with the depth estimation results mentioned by Salem and Ravat (2003), as well as with previous research in this field (Abadi, 2020). As a result, the anomaly depth in the northern region is shallower than in the southern one. Gravity data results show an overall minimum and maximum depth diffusion ranging from 49 to 145 m across the entire area, as well as the depth estimates from magnetic data with

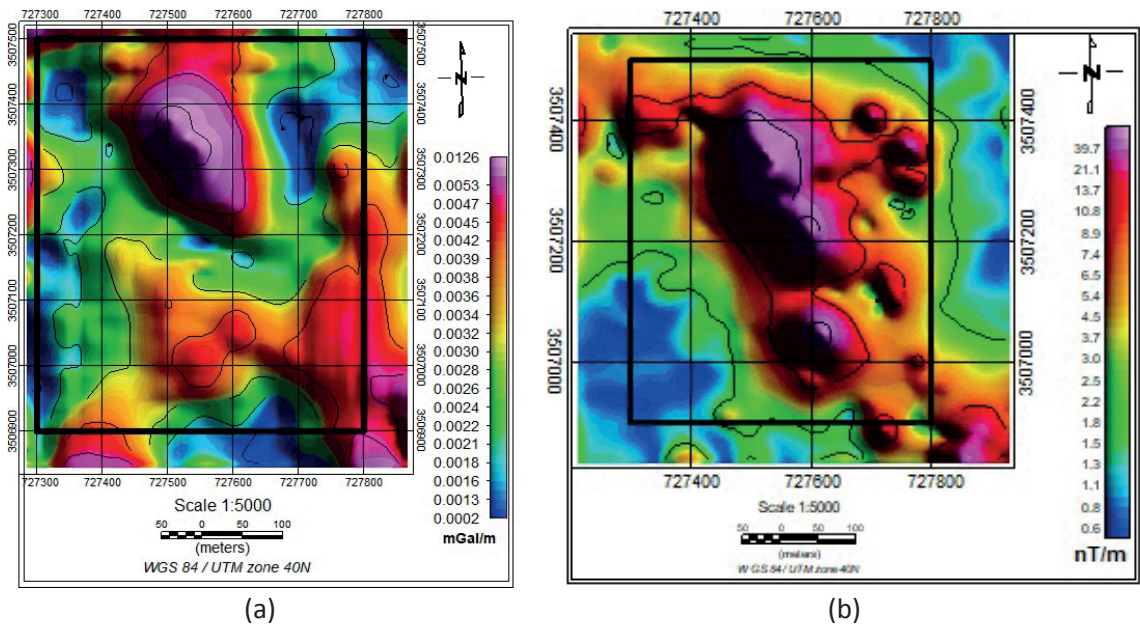


Fig. 26 - Analytical signal of upward continued potential field data: a) gravity data, and b) magnetic data, where black polygons indicate the selected area for executing the proposed depth estimation algorithm.

overall values ranging from 36 to 92 m. Of note is the fact that the maximum frequency of the solutions, both for the magnetic and gravity potential fields, ranges from 40 to 60 m, consistently with the geological information of the study area and previous research results.

As illustrated in Figs. 28c and 28d, several different sized windows, in different areas of the mesh, were tested, leading to acceptable estimates based on the input tolerance range.

Noticeably, in the southern part of the potential anomaly (south of the fault), within the black polygon (see Fig. 29), Fig. 28a shows that the Euler depth estimates for gravity data returned deeper estimates rather than the Euler solutions for magnetic data (it almost shows a bigger and deeper mass). For this reason, the optimal Euler windows, with minimum uncertainty, become larger for gravity data, and smaller for magnetic data (Figs. 28c and 28d). Meanwhile, the uncertainty of the depth solutions also falls within the expected error range (Figs. 28e and 28f), as reasonably expected due to the different drops of the gravity and magnetic potential fields.

On closer inspection in the northern part of the grey polygon anomaly, the match between the Euler results, of the magnetic and gravity data, is improved, despite the different sampling distance and lower resolution of the gravity data (Figs. 28a and 28b). The optimal window results for the magnetic data in the grey polygon region, and the comparison with the analytical signal edge detection filter, show that the optimal window in this region is larger than the purple polygon region (Figs. 28b and 29b). The difference in optimal window size is due to the fact that the purple polygon area has a smaller and deeper structure, and, consequently, it has smaller optimum windows compared to the grey polygon area. The region, separated by the grey polygon, shows a larger, shallower structure with larger optimal windows (Fig. 28b). The results of the gravity data in this region indicate that the optimal windows include medium and large values, and the average window size values are located at the edges, which may be due to the lower resolution of the gravity data along with the lower drop of the gravity potential field data (Fig. 28a).

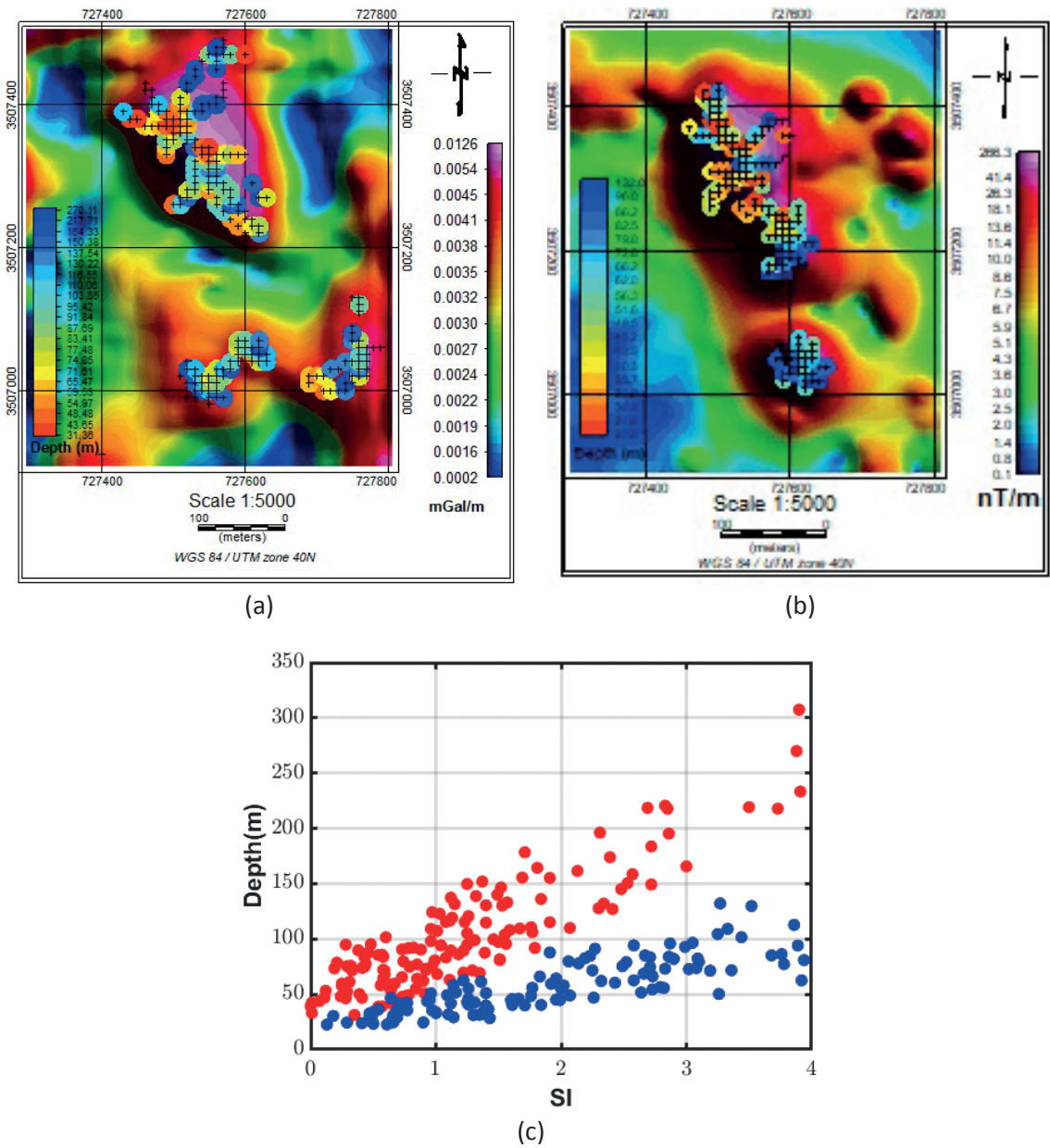


Fig. 27 - Depth estimation over peak points of the analytic signal map of: a) gravity, b) magnetic data on the Shavaz iron-bearing deposit, and c) plot of the average depth versus the *SI* estimates for gravity data (red circles), and magnetic data (blue circles).

In summary, the difference in the behaviour of the Euler depth estimation in the case of the two potential fields of gravity and magnetic data may be due to the different nature of the data, to the different resolution obtained in magnetic or gravity data survey, as well as to differences in distance, which lead to different decay rates of the gravity and magnetic potential fields (Fig. 22). Other influencing factors may be the different detection capability or the greater sensitivity of the magnetic method to underground changes in the physical properties of the subsurface structures, or the different physical properties (density and susceptibility) of the subsurface

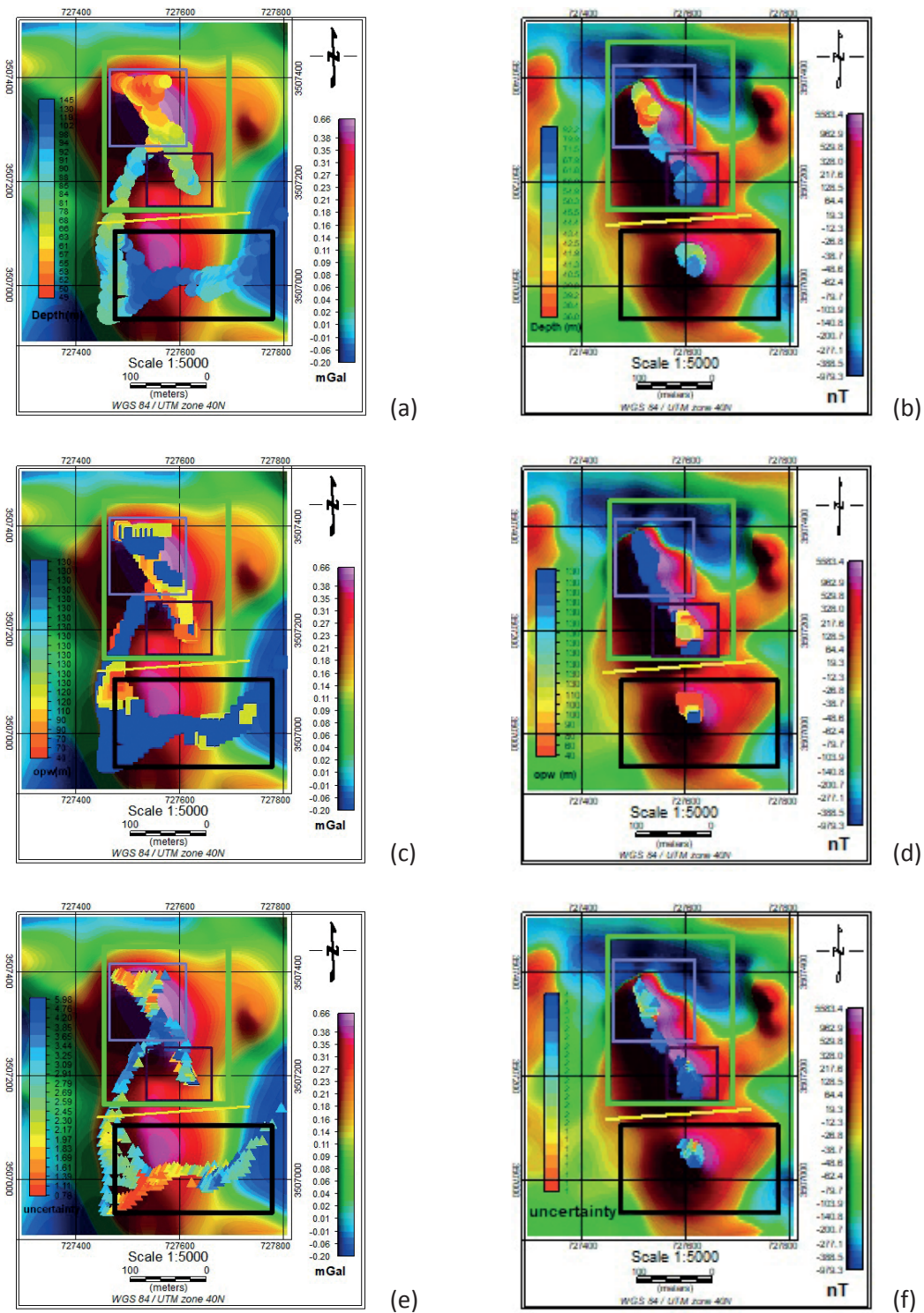


Fig. 28 - Depth estimation of the potential field survey on the Shavaz iron-bearing deposit, where the left column is for gravity and the right column is for magnetic data. The top row illustrates depth estimation for: a) gravity, and b) magnetic data. The middle row shows the optimum window size for: c) gravity, and d) magnetic data. The bottom row presents the uncertainty for: e) gravity, and f) magnetic data (the coloured polygons indicate the boundaries separated by the analytic signal edge detection filter, and the yellow line indicates a major E-W fault in the studied region).

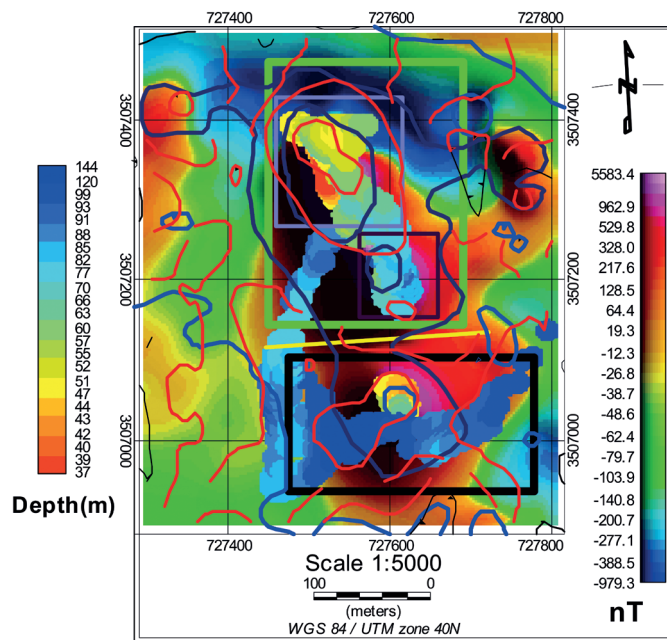


Fig. 29 - Depth solutions and contour lines of the potential field analytical signal filter over the residual magnetic map, where the red contour lines indicate gravity data and the blue ones magnetic data. Coloured polygons show the separated areas.

masses along with the different signal-to-noise data ratio. Therefore, the combination of results from gravity and magnetic data sets can provide better conclusions in Euler depth estimation and other geophysical methods. For this reason, this study used both of the mentioned potential fields together. This is worth further investigation in future research.

In Fig. 29, the dynamic Euler solution, for the two potential fields is displayed simultaneously on the magnetic map along with the contour lines of the analytical signal for the potential field that precisely separate the boundaries of the structures, providing an interpretational view for the Euler depth solutions.

6. Conclusions

The Euler deconvolution method is a well-known practical tool for interpreting potential field geophysics data. For the results to match reality, the input parameters must be realistically and precisely determined. Solving the Euler equation and choosing the appropriate window size have always been a challenge due to the emergence and existence of various sources with different dimensions and depths. Considering different window sizes, from a minimum to a maximum value, in different areas of the grid, the proposed algorithm calculates the Euler equation solutions to obtain the best responses with minimum uncertainty. The final depth solutions of the equations are also automatically checked against input tolerances.

To investigate the validity and accuracy of the proposed algorithm, several synthetic scenarios were simulated. The results concur well with the original models, and the algorithm is able to recover acceptable depth distributions for both homogenous and inhomogeneous potential field sources. For each model, the average S/s were estimated using analytic signal peaks, which

were, then, used as input to the Euler equation. Synthetic model simulation results indicate that, in each area of the mesh, a dynamic window of different sizes shows great improvement in generating acceptable results with initial tolerance range entries. The proposed dynamic window technique is also compared with the fixed window method, which demonstrates the completeness of the algorithm.

After obtaining the desired results on the synthetic models of magnetic and gravity sources, the algorithm was used for real field data in the Shavaz region, and the results obtained proved to match closely with current geological information and previous studies. The proposed algorithm and research solution are almost able to reduce the interpreters' challenge, or possible mistakes, in choosing a fixed window size for the entire grid. A series of dimensions for each area of the grid are used to solve the equations with minimum uncertainty considering error tolerance.

This method allows to illustrate and visualise a range of magnetic and gravity depth solutions, which are quite accurate, and to obtain a view of the spatial distribution of the solutions to compare, combine, and check the investigation of subsurface geological features.

Acknowledgments. The authors express their sincere thanks to the Institute of Geophysics and the School of Mining Engineering, University of Tehran, as well as to the Department of Mining and Metallurgical Engineering, Amirkabir University of Technology, for all the support provided.

REFERENCES

- Abedi M.; 2020: *A focused and constrained 2D inversion of potential field geophysical data through Delaunay triangulation, a case study for iron-bearing targeting at the Shavaz deposit in Iran*. Phys. Earth Planet. Inter., 309, 106604, 14 pp., doi: 10.1016/j.pepi.2020.106604.
- Afshar A., Norouzi G.H., Moradzadeh A., Riahi M.A. and Porkhial S.; 2017: *Curie point depth, geothermal gradient and heat-flow estimation and geothermal anomaly exploration from integrated analysis of aeromagnetic and gravity data on the Sabalan area, NW Iran*. Pure Appl. Geophys., 174, 1133-1152.
- Agard P., Omrani J., Jolivet L., Whitechurch H., Vrielynck B., Spakman W., Monié P., Meyer B. and Wortel R.; 2011: *Zagros orogeny: a subduction-dominated process*. Geol. Mag., 148, 692-725.
- Aster R.C., Borchers B. and Thurber C.H.; 2018: *Parameter estimation and inverse problems, 3rd ed.* Elsevier, Amsterdam, The Netherlands, 392 pp.
- Barbosa V.C., Silva J.B. and Medeiros W.E.; 1999: *Stability analysis and improvement of structural index estimation in Euler deconvolution*. Geophys., 64, 48-60.
- Chen T. and Zhang G.; 2018: *Forward modeling of gravity anomalies based on cell mergence and parallel computing*. Comput. Geosci., 120, 1-9.
- Fedi M.; 2016: *An unambiguous definition of the structural index*. In: Expanded Abstracts SEG Technical Program, Society of Exploration Geophysicists, Dallas, TX, USA, pp. 1537-1541.
- Fedi M., Florio G. and Paoletti V.; 2015: *MHODE: a local-homogeneity theory for improved source-parameter estimation of potential fields*. Geophys. J. Int., 202, 887-900.
- Gerovska D. and Araúzo-Bravo M.J.; 2003: *Automatic interpretation of magnetic data based on Euler deconvolution with unprescribed structural index*. Comput. Geosci., 29, 949-960.
- Ghahamghash J. and Mohammadiha K.; 2005: *Geological map of Kafeh-e-Tagestan, Iran, Scale 1:100,000*. Geological Survey and Mineral Exploration of Iran, Tehran, Iran.
- Ghiasi S.M., Hosseini S.H., Afshar A. and Abedi M.; 2023: *A novel magnetic interpretational perspective on Charmaleh Iron Deposit through improved edge detection techniques and 3D inversion approaches*. Nat. Resour. Res., 32, 147-170, doi: 10.1007/s11053-022-10135-7.
- Guo C.C., Xiong S.Q., Xue D.J. and Wang L.F.; 2014: *Improved Euler method for the interpretation of potential data based on the ratio of the vertical first derivative to analytic signal*. Appl. Geophys., 11, 331-339.
- Hosseini S.H., Dehkordi H.B., Abedi M. and Oskooi B.; 2021: *Implications for a geothermal reservoir at Abgarm, Mahallat, Iran: magnetic and magnetotelluric signatures*. Nat. Resour. Res., 30, 259-272.
- Melo F.F. and Barbosa V.C.; 2018: *Correct structural index in Euler deconvolution via base-level estimates*. Geophys., 83, J87-J98, doi: 10.1190/geo2017-0774.1.

- Meyer B., Mouthereau F., Lacombe O. and Agard P.; 2006: *Evidence of Quaternary activity along the Deshir Fault: implication for the Tertiary tectonics of central Iran*. Geophys. J. Int., 164, 192-201.
- Reid A.B. and Thurston J.B.; 2014: *The structural index in gravity and magnetic interpretation: errors, uses, and abuses*. Geophys., 79, J61-J66, doi: 10.1190/GEO2013-0235.1.
- Reid A.B., Allsop J.M., Granser H., Millett A.T. and Somerton I.W.; 1990: *Magnetic interpretation in three dimensions using Euler deconvolution*. Geophys., 55, 80-91.
- Reid A.B., Ebbing J. and Webb S.J.; 2014: *Avoidable Euler errors - the use and abuse of Euler deconvolution applied to potential fields*. Geophys. Prospect., 62, 1162-1168.
- Salem A. and Ravat D.; 2003: *A combined analytic signal and Euler method (AN-EUL) for automatic interpretation of magnetic data*. Geophys., 68, 1952-1961.
- Shafiei B.; 2010: *Lead isotope signatures of the igneous rocks and porphyry copper deposits from the Kerman Cenozoic magmatic arc (SE Iran), and their magmatic-metallogenic implications*. Ore Geol. Rev., 38, 27-36.
- Thompson D.T.; 1982: *EULDPH: a new technique for making computer-assisted depth estimates from magnetic data*. Geophys., 47, 31-37.

Corresponding author: Maysam Abedi
School of Mining Engineering, College of Engineering, University of Tehran
Amirabad, Tehran 98, Iran
Phone: +98 21 6111 4563; e-mail: maysamabedi@ut.ac.ir